IGAM/UG Technical Report for ESA/ESTEC No. 2/2002

ESA study:

ACE Scientific Support Study

[ESA/ESTEC Contract No. 14809/00/NL/MM, WP3300: Error Analysis for Climate Applications; Part WP3300]

Sensitivity of Atmospheric Profiles Retrieved from GNSS Occultation Data to Horizontal Variability in the Troposphere

by

U. Foelsche and G. Kirchengast
(IGAM/University of Graz, Graz, Austria)

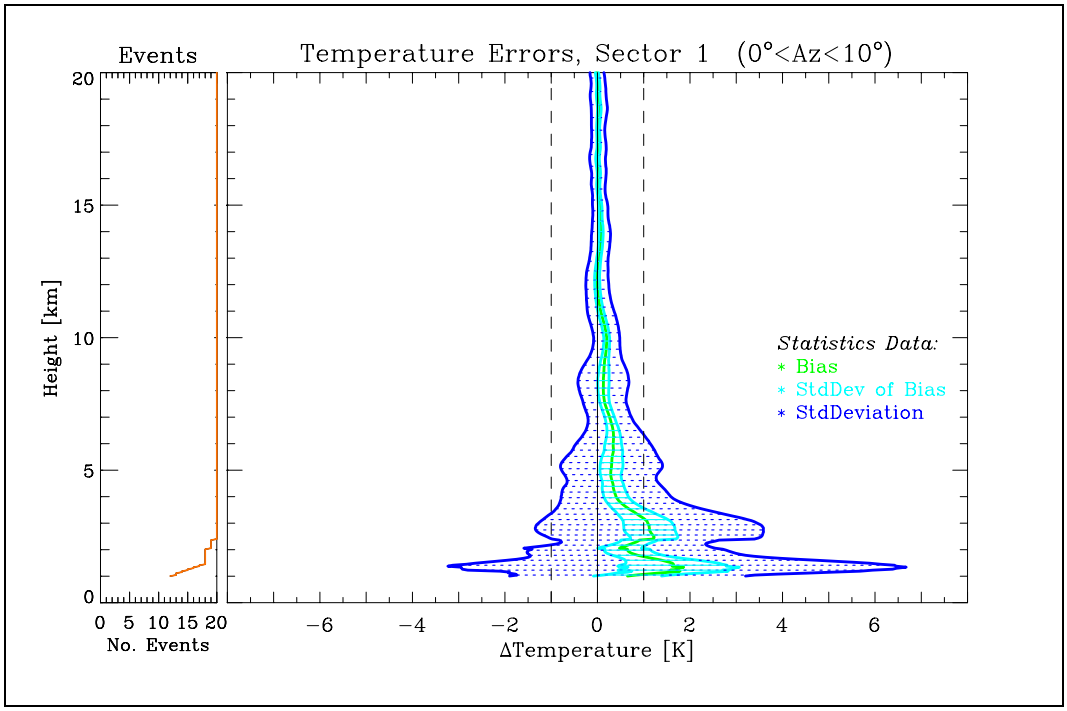

January 2002

Table of Contents

1. Introduction

This report deals with part of Work Package 3000 (WP 3000) of the ACE Scientific Support Study (Hoeg et al., 2000). WP 3000 is dedicated to the error analysis of Global Navigation Satellite System (GNSS) radio occultation (RO) measurements for climate applications.

1.1. Study Objectives

The part addressed by this report, WP 3300, investigates the sensitivity of atmospheric profiles retrieved from RO data to atmospheric horizontal variability errors in a twofold manner: First, the error of a (realistic) horizontally variable atmosphere relative to a spherically symmetric atmosphere is quantified based on an ensemble of occultation events (using an European Centre for Medium-Range Weather Forecasts, ECMWF, T213L50 analysis field with and without horizontal variability). The difference incurred by either assuming the "true" profile vertically at a mean event location (the common practice) or more precisely along the estimated 3D tangent point trajectory traced out during the event is assessed in this context as well. Second, the sensitivity of retrieval products to the angle-of-incidence of occultation rays relative to the boresight direction of the receiving antenna (aligned with the LEO orbit plane) is analysed based on ensembles of events (from the same ECMWF analysis field) for three different angle-of-incidence classes (±10 deg, ±20 to ±30 deg, ±40 to ±50 deg). This provides important insights into how much the climate monitoring utility of GNSS occultation data depends on occultation event geometry.

1.2. Study Overview

The EGOPS software tool (End-to-end GNSS Occultation Performance Simulator, version 4.0) was used to generate realistically simulated measurements of the observables bending angle, refractivity, total atmospheric pressure, geopotential height, and (dry) temperature. A brief description of the EGOPS tool can be found in the companion report on WP 3200 by Gobiet and Kirchengast (2001), for more detailed descriptions of EGOPS see Kirchengast (1998) and Kirchengast *et al.* (2001). Section 2 gives an overview on the experimental setup. Results on the sensitivity to horizontal variability are presented in section 3, the results on sensitivity to angle-of-incidence are shown and discussed in section 4. Conclusions and an outlook are finally provided in section 5. Furthermore, the input parameter files involved in the EGOPS simulations are collected in Appendix A, enabling a detailed view on the simulation conditions adopted, while Appendix B contains a catalogue of all (dry) temperature profiles obtained in the study, allowing detailed inspection of features of individual events.

2. Experimental Setup

2.1. Geometry

We assumed a full constellation of 24 Global Positioning System (GPS) satellites as transmitters and a GRAS (GNSS Receiver for Atmospheric Sounding) sensor onboard the nominal METOP orbit (altitude ~830 km). The corresponding orbital elements are listed in

Appendix A.1 in the form of "Two Line Element" (TLE) sets. With such a constellation a total of somewhat over 500 occultation events per day is obtained during a simulation over a 24 hour period. The simulated day was September 15, 1999, as the ECMWF analysis field to be used in the subsequent forward modeling is associated with this day.

We collected occultation events in three different azimuth sectors relative to the boresight direction of the receiving antennae. A schematic illustration of this division into several "angle-of-incidence" sectors is given in Figure 1, while Table 1 summarizes the simulation design in terms of numbers of events simulated per sub-sector defined. Sector 1 (indicated dark gray in Figure 1 and Table 1) comprises azimuth angles between -10° and +10° (rising occultation) plus angles between 170° and 190° (setting occultations). Angles of incidence in the range of |25°| ±5°, symmetric to the orbit plane, compose Sector 2 (four medium gray sub-sectors in Figure 1 and in Table 1). Sector 3 corresponds to angles of incidence in the range of |45°| ±5°, symmetric to the orbit plane (light gray in Figure 1 and Table 1). As an example for how these events have been geometrically defined, EGOPS "Mission Analysis/Planning" input specifications for a sub-sample (setting events, azimuth = 135° ±5°; rising events: azimuth = 45° ±5°) are listed in Appendix A.2.

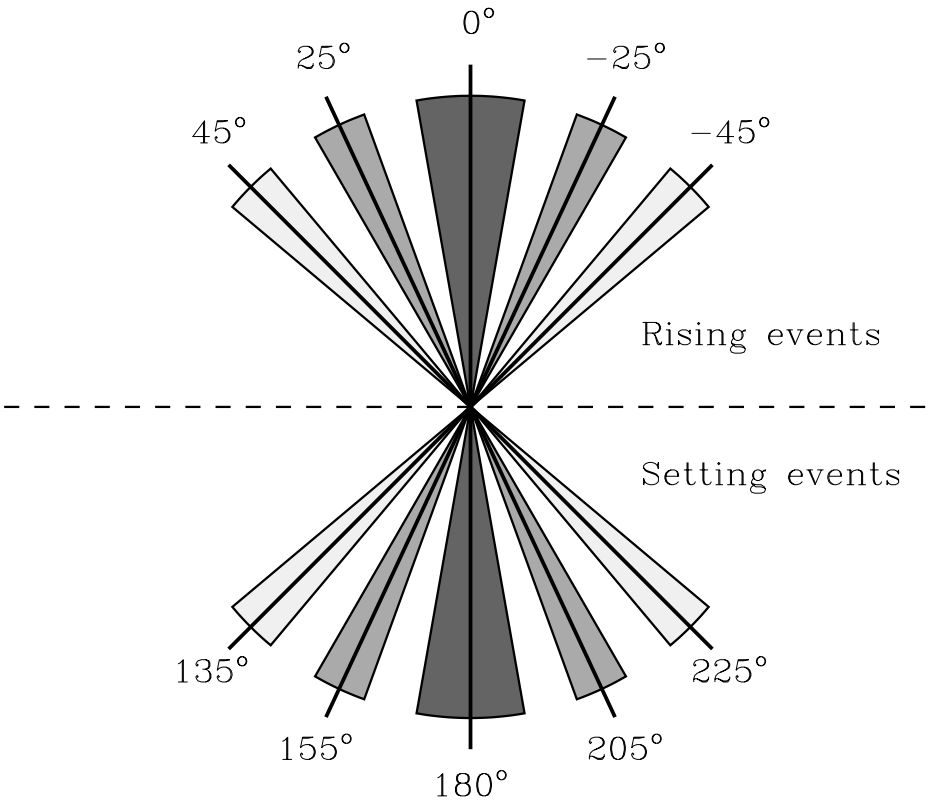

Fig. 1. Schematic illustration of azimuth sectors used in the study: sector 1 (dark gray), sector 2 (medium gray), and sector 3 (light gray).

	Sector 1	Sector 2	Sector 3	No. of Events
Rising events	0° to –10°	–20° to –30°	–40° to –50°	15
	0° to +10°	+20° to +30°	+40° to 50°	15
Setting events	170° to 180°	150° to 160°	130° to 140°	15
	180° to 190°	200° to 210°	220° to 230°	15
No. of events	20	20	20	**60**

Table 1. Azimuth sectors used in this study. We selected 5 rising or 5 setting events, respectively, in each of the 12 sub-sectors, leading to a total ensemble of 60 events.

With restriction to the described azimuth sectors we obtained a total of 321 occultation events during the selected 24 hour period. The geographic distribution is shown in the top panel of Figure 2. From the sample of about 320 occultations we selected 20 events per azimuth sector (60 events in total) in order to keep computational expenses limited. Selection criteria were:

- Uniform distribution in latitude (and, if possible, in UT) in each sector.
- Equal density over oceans and over continents in each sector.
- Five occultation events in each sub-sector (same amount of rising and setting occultations; see also Table 1).

The geographic distribution of the 60 selected occultation events is displayed in the bottom panel of Figure 2. It is visible that a reasonably representative coverage is achieved with the selected ensemble.

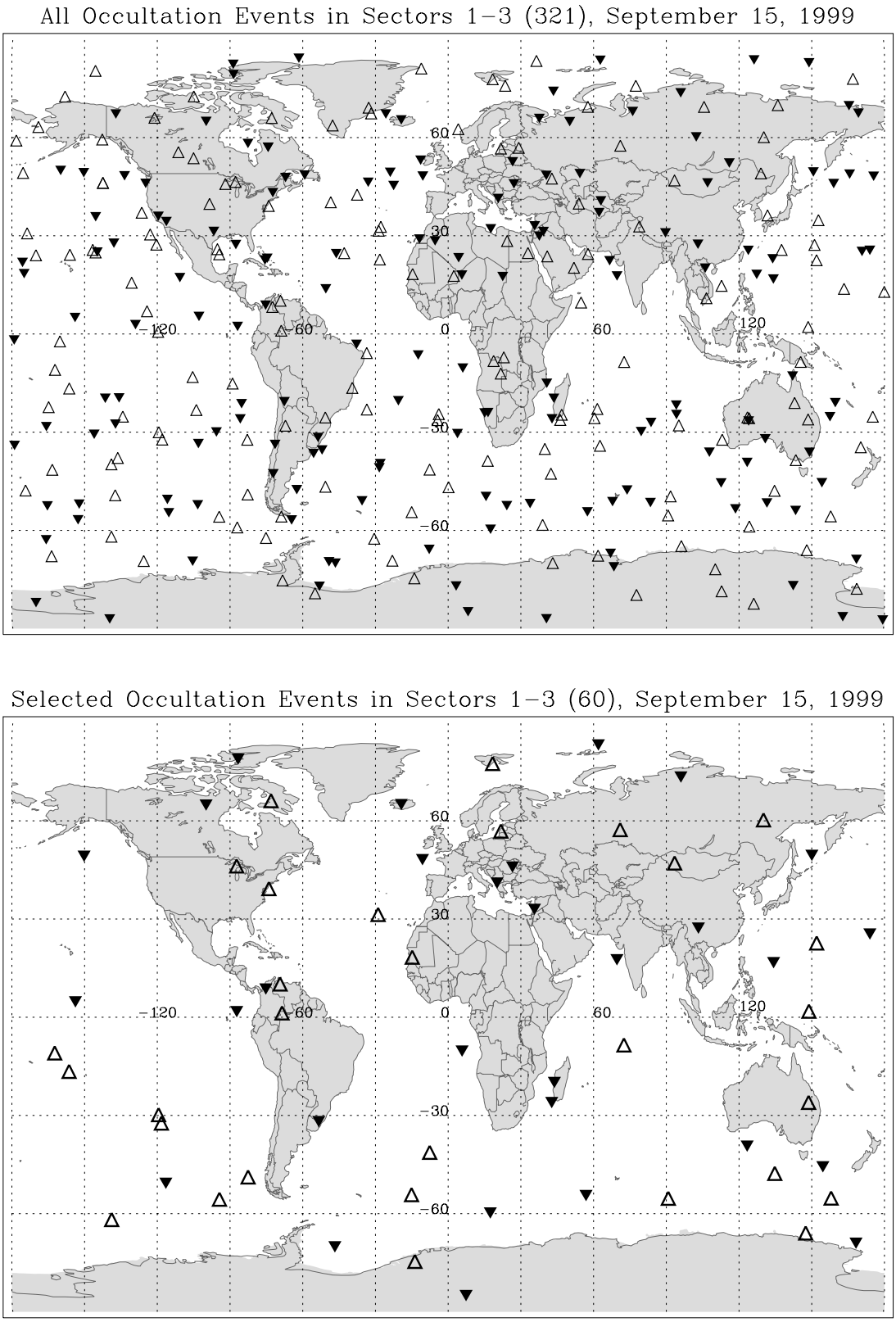

Fig. 2. Locations of occultation events during one day in all three azimuth sectors. Top panel: all events, bottom panel: selected events (20 in each sector). Upright open triangles denote rising occultations. Upside-down filled triangles denote setting occultations.

2.2. Forward Modeling

High resolution (T213L50) analysis fields from the European Centre for Medium-Range Weather Forecasts (ECMWF) for September 15, 1999, 12 UT, were used to generate realistic atmospheric phase delays. The horizontal resolution (T213) corresponds to 320 times 640 points in latitude and longitude, respectively, and thus furnishes several grid points within the typical horizontal resolution of an occultation event of ~300 km (e.g., Kursinski *et al.*, 1997). This sufficiently dense sampling is important to have quasi-realistic representation of horizontal variability errors, the investigation of which is the focus of this report. In the vertical, 50 levels (L50, hybrid pressure coordinates) extend from the surface to 0.1 hPa, being most closely spaced in the troposphere, which represents good vertical sampling. In order to illustrate the quasi-realistic temperature and humidity structure contained in the T213L50 field utilized, slices of specific humidity and temperature are displayed in Figure 3.

The MSIS climatological model (Hedin, 1991) was used, with a smooth transition from the ECMWF analysis field upwards, above the vertical domain of that field. As we focused on the troposphere, we made the reasonable assumption that ionospheric residual errors can be neglected (Steiner *et al.*, 1999). Forward modeling was therefore employed without ionosphere, which corresponds to considerable savings in computational expenses.

We performed high-precision 3D ray tracing with sub-millimetric accuracy and a sampling rate of 10 Hz for all forward modeled events through the ECMWF analysis. In order to be able to compare the ensemble of measurements subjected to horizontal variability with one without horizontal variability, two separate ensembles of 60 events were forward modeled: One with employing the analysis field with its 3D structure as is, the other with artificially enforcing spherical symmetry for all events. The latter case was obtained by applying the atmospheric profile at the mean tangent point of an occultation event over the entire domain probed. As an example for showing how these forward simulations have been defined, EGOPS "Forward Modeling" input specifications for one sub-sample of 5 occultations (setting events, azimuth = 135°±5°) are listed in Appendix A.3.; in this input parameter listing the two alternatives (horizontal variability or spherical symmetry, respectively) are highlighted.

As in the real atmosphere, occultation events over oceans at low latitudes occasionally failed to penetrate the lowest ~4 km of the troposphere (in the present simulations, the reason is that the ray tracer encounters superrefractive structures, which it cannot "overcome"). All 60 events included in the final ensemble and used for computing the statistical results reached to a minimum height of ~2 km or closer to the surface. The retrieval processing (section 2.3) led, for individual events, to a further increase of the minimum height reached (see result figures in sections 3 and 4).

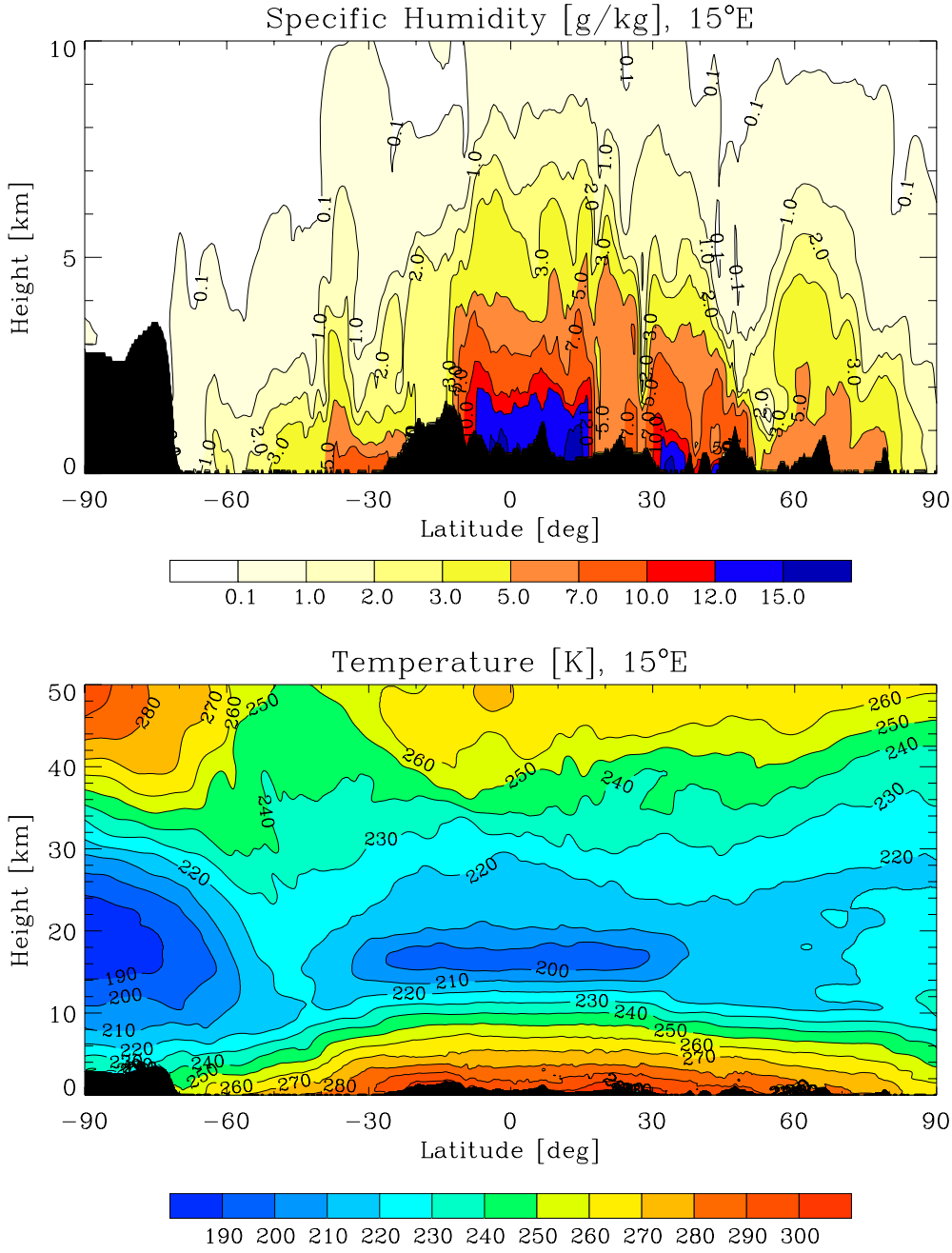

Fig. 3. Latitude-versus-Height slices at 15° eastern longitude, September 15, 1999, 12 UT (T213L50 ECMWF analysis field). Top panel: specific humidity in units [g/kg], bottom panel (different height range): temperature in units [K].

2.3. Observation System Modeling and Retrieval Processing

Realistic errors (including error sources like orbit uncertainties, receiver noise, local multipath errors and clock errors) have been superimposed on the obtained simulated phase measurements. For this realistic receiving system simulation, we reflected (conservatively) the specifications and error characteristics of the GRAS instrument (e.g., GRAS-SAG, 1998). For

information, the corresponding EGOPS "Observation System Modeling" input specifications (for the horizontal variability case, as an example) are listed in Appendix A.4.

Regarding retrieval processing, we applied both geometric optics and wave optics bending angle retrieval schemes in course of the analysis and compared their performance. Based on the comparison we decided to use for this study the results of the geometric optics bending angle retrieval scheme, more specifically, of the "enhanced bending angle retrieval" algorithm of EGOPS. The core of this algorithm, transforming phase delays to bending angles, is the algorithm described by Syndergaard (1999), which was enhanced to include inverse covariance weighted statistical optimization (with prior best-fit a priori profile search) as described in the companion report by Gobiet and Kirchengast (2001). Since Forward Modeling has been performed without ionosphere, ionospheric correction was trivial. The wave optics scheme considered employs backpropagation followed by a canoncial transform, which is currently the most advanced bending angle retrieval concept for the troposphere. The algorithm tested was the one described by Gorbunov (2001a; 2001b), which was very recently implemented in a prototype mode in EGOPS. As the results indicated that some tuning of the implementation is still necessary (small residual offsets and differences between set and rise events were observed) we did not further utilize them in this report.

Refractivity profiles have been computed using a standard Abel transform retrieval employing the EGOPS-internal algorithm of Syndergaard (1999). Profiles of total atmospheric pressure and temperature, respectively, have been obtained using a standard dry air retrieval algorithm as again developed by Syndergaard (1999). Geopotential height profiles where obtained by converting geometrical heights z of pressure levels via the standard relation $dZ = (g(z,\varphi)/g_0)dz$ (e.g., Salby, 1996) to geopotential heights Z, where $g(z,\varphi)$ invokes the international gravity formula (e.g., Landolt-Börnstein, 1984) and $g_0 = 9.80665$ ms^{-2} is the standard acceleration of gravity. We did not undertake to separately analyze temperature and humidity, e.g., by the EGOPS-internal optimal estimation algorithm following Healy and Eyre (2000), since for this baseline analysis of horizontal variability errors it was decided (Hoeg et al., 2000) to inspect variables such as refractivity and dry temperature, which do not have mixed in any prior information.

Appendix A.5 summarizes the EGOPS "Inversion/Retrieval" input specifications corresponding to the retrieval processing chain applied (for the same exemplary sub-sample as Appendix A.4).

2.4. Reference Profiles

For the results shown in sections 3 and 4, all the retrieved profiles of bending angle, refractivity, pressure, geopotential height, and temperature, respectively, have been differenced against the corresponding "true" ECMWF vertical profiles at mean tangent point locations, also termed reference profiles. The differences incurred by either assuming the reference profile vertically at a mean event location (the common practice) or more precisely along the estimated 3D tangent point trajectory traced out during the event has been assessed as well (within section 3).

As described in section 2.3, pressure and temperature profiles were computed, assuming a dry atmosphere, based on standard formulae (Syndergaard, 1999). We consequently compare to "true" (dry) pressure, (dry) geopotential height, and dry temperature profiles from the

ECMWF field. This implies that the temperature profiles have increasingly subsumed moisture effects below 10 km. The dependence of dry temperature on actual temperature and humidity is accurately known via the refractivity formula (Smith and Weintraub, 1953), however, so that one can always track the degree of influence of moisture if desired.

Actual "true" bending angle profiles have not been available for this study (planned to be available in a next version of EGOPS). Thus the reference bending angle profiles have been computed by applying a forward Abel transform (e.g., Syndergaard, 1999; Rieder and Kirchengast, 2001a) to the corresponding "true" refractivity profiles. Since this Abelian estimation involves the assumption of spherical symmetry, the resulting "approximately true" bending angles as function of impact parameter deviate from the actual "true" ones from propagation through the full 3D-variable refractivity field. The present bending angle error estimates thus have to be interpreted with care, particularly below 5 km, where horizontal inhomogeneities are most important. Following future upgrade of EGOPS to rigorously supply "true" bending angles as a by-product of forward modeling, a refinement of the bending angle error results is foreseen.

3. Sensitivity to Horizontal Variability Errors

In this part of the study we focused on the influence of horizontal variability. Results for the "real" atmosphere with horizontal variability are therefore compared with the results for the artificial spherically symmetric atmosphere (bottom and middle panels of Figures 4 to 8). Furthermore, differences between "true" vertical profiles and "true" profiles extracted along the 3D tangent point trajectories (the latter taken as reference) are shown (bottom panels of Figures 4 to 8). The results for the full ensemble of 60 events are illustrated in all panels. The gradual decrease in the number of events towards lower tropospheric levels (small left-hand-side subpanels) is due to the different minimum heights reached by individual events.

Differencing of retrieved profiles with co-located reference profiles allows computation of the total bias errors and standard deviations in the parameters under investigation. The exponential decrease of bending angle, refractivity, and pressure with height inhibits the visual representation of absolute errors. Errors in refractivity (Figure 4), pressure (Figure 5), and bending angle (Figure 8) are thus shown as relative errors in units [%], while geopotential height (Figure 6) and dry temperature errors (Figure 7) are displayed in units [gpm] and [K], respectively. All statistics are shown between 1 km and 20 km above (ellipsoidal) surface; dashed vertical lines mark relative errors of 0.5 % and absolute errors of 10 gpm and 1 K, respectively.

3.1. Refractivity Errors

Figure 4 illustrates that refractivity errors in a horizontally variable atmosphere increase considerably below a height of about 7 km (top panel). In the spherically symmetric atmosphere (middle panel), the increase in refractivity error is significantly less pronounced. Above 7 km, the overall behavior is quite smooth; there is a small negative bias of about 0.1%, standard deviations under horizontal variability (spherical symmetry) increase from ~0.17% (~0.14%) at 20 km to ~0.38% (~0.30%) at 7 km.

Below 7 km there is considerable structure in the error profiles. In the spherically symmetric atmosphere, standard deviations reach maximum values of about 1% at heights around 2.5 km, with a maximum (negative) bias of 0.26%. In the realistic atmosphere, standard deviations reach a maximum value of 1.75% at 1.8 km height, the bias slightly exceeds 0.5% around 2.5 km and below 1.7 km.

3.2. Dependence on Geometry of Reference Profiles

According to Figure 4 (bottom panel), differences between "true" vertical profiles at mean tangent point locations and "true" ones along actual 3D tangent point trajectories are very small in the lower stratosphere, since the EGOPS mean location estimate is designed to fit best around 15 km. Below 7 km, however, the differences are of a magnitude comparable to the errors estimated under horizontal variablility (top panel). This implies that the geometrical mis-alignment of the actual tangent point trajectory with the mean-vertical contributes as a major source to horizontal variability error. Additional visual evidence for this is that the bias below 7 km in the lower panel appears roughly mirror-symmetric relative to the one in the upper panel: this occurs since the geometrical mis-alignment is a main bias source in both cases so that a clearly visible effect left is the change in sign due to the upper panel using the mean-vertical profile as reference while the lower panel uses the along-trajectory one.

This finding applies also to the other parameters (Figures 5 to 8) and indicates the importance of utilizing tropospheric RO profiles not just vertically but as good as possible consistent with the actual tangent point trajectory (or, more generally, occultation plane movement). Appendix B, which illustrates for temperature the full set of individual profiles involved in order to enable inspection event by event, further supports this statement by exhibiting, for most events, quite smaller differences in the troposphere between retrieved and along-trajectory profiles than between retrieved and mean-vertical ones. Overall, the results show that the performance in the realistic horizontally variable troposphere is markedly improved if measured against the actual tangent point trajectory.

Future work will investigate this matter more closely based on an even higher-resolved field (ECMWF T511L60 analysis field) and will also rigorously inspect by how much the applicable rms and bias errors decrease if the data are exploited along a tangent point trajectory deduced purely from observed data, mainly GNSS and LEO satellite position and bending angle data.

3.3. Pressure Errors

The pressure errors (Figure 5) display a similar behavior as the refractivity errors, though the smaller-vertical-scale variations are less pronounced due to the hydrostatic integration.

In the spherical symmetry case, all relative errors increase with decreasing height (bias from 0.04% to 0.17%, standard deviation from 0.15% to 0.38%). In the realistic atmosphere with horizontal variability, standard deviations are smallest around 13 km height (0.16%), below they increase up to ~0.5% around 1.3 km height, where the negative bias also has its maximum value of ~0.2%.

3.4. Geopotential Height Errors

Errors in the geopotential height of pressure surfaces are shown in Figure 6 as function of pressure height z_p (a convenient pressure coordinate defined as $z_p = -7 \cdot \ln(p[\text{hPa}]/1013.25)$, which is closely aligned with height z). Mirroring the pressure errors (see, e.g., Syndergaard, 1999, on the relation between pressure and geopotential height), positive biases in geopotential height correspond to negative biases in pressure (cf. Figures 5 and 6).

In the realistic atmosphere, biases are < 5 gpm above about 7 km, exceed 10 gpm below about 3 km, and reach a maximum of ~13 gpm at ~1.3 km pressure height (corresponding to a pressure error of ~0.2%). Standard deviations are < 15 gpm above about 5 km and reach ~33 gpm at lowest levels. In the spherically symmetric atmosphere, the bias above about 7 km is largely the same as in the realistic case, but remains < 8 gpm lower down (compared to ~13 gpm with horizontal variability); the standard deviation reaches ~20 gpm (instead of ~33 gpm) at lowest levels.

3.5. Temperature Errors

The dry temperature errors are depicted in Figure 7. In the scenario with horizontal variability, all errors below 7 km are larger than the corresponding errors under spherical symmetry. A positive bias of ~1 K is reached around 2.6 km, 1.5 km, and 1.2 km, respectively, where standard deviations of about 4 K are encountered.

Under spherical symmetry, the maximum bias is < 0.4 K at 1.6 km, standard deviations remain smaller than ~2.5 K. Between 7 km and 20 km there is essentially no temperature bias in both scenarios (i.e., always smaller than 0.1 K). Appendix B allows detailed event-by-event inspection of all temperature profiles involved.

3.6. Bending Angle Errors

The bending angle errors are shown in Figure 8 as function of impact height (impact parameter minus local radius of curvature). Their major characteristics in terms of height dependence are similar to those of the refractivity errors (Figure 4). The magnitude of relative errors is generally around a factor of 2 higher, however, and even more than this below 5 km. This occurs mainly since the Abel inversion employed involves smoothing, which increases the accuracy (but also somewhat degrades resolution).

The error results, in particular those below 5 km, are presumably somewhat too conservative, since we used "true" bending angle estimates derived under spherical symmetry conditions from the "true" refractivity profiles instead of realistic "true" bending angles from 3D ray tracing (as noted in section 2.4 in more detail). This approximation will be avoided in future more rigorous bending angle error assessments based on enhanced forward modeling, which will include the computation of "true" bending angles via high-precision 3D ray tracing.

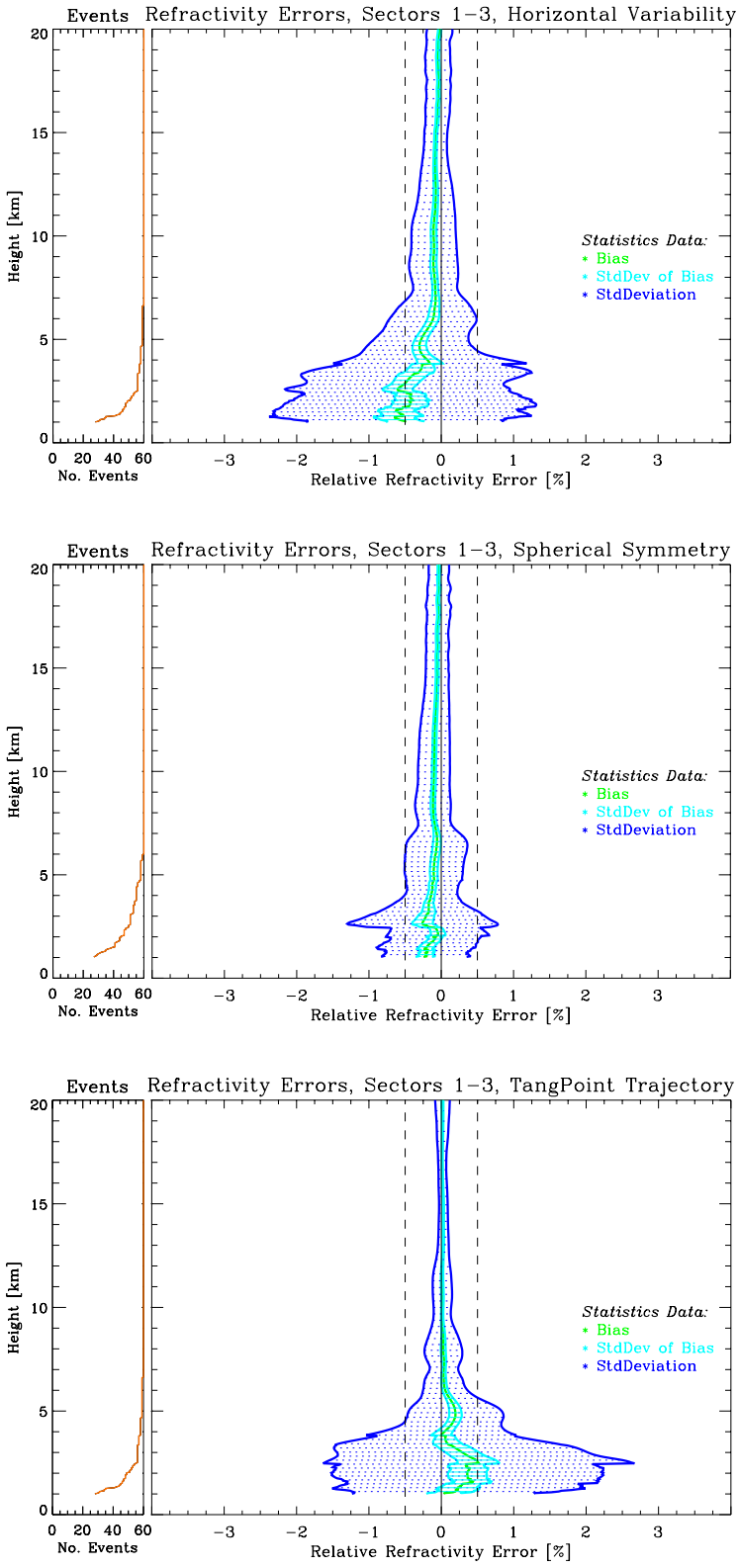

Fig. 4. Refractivity error statistics for the ensemble of all 60 occultation events in all sectors. Top panel: atmosphere with horizontal variability; middle panel: atmosphere with spherical symmetry applied; bottom panel: difference vertical profile at mean tangent point–minus–along 3D tangent point trajectory.

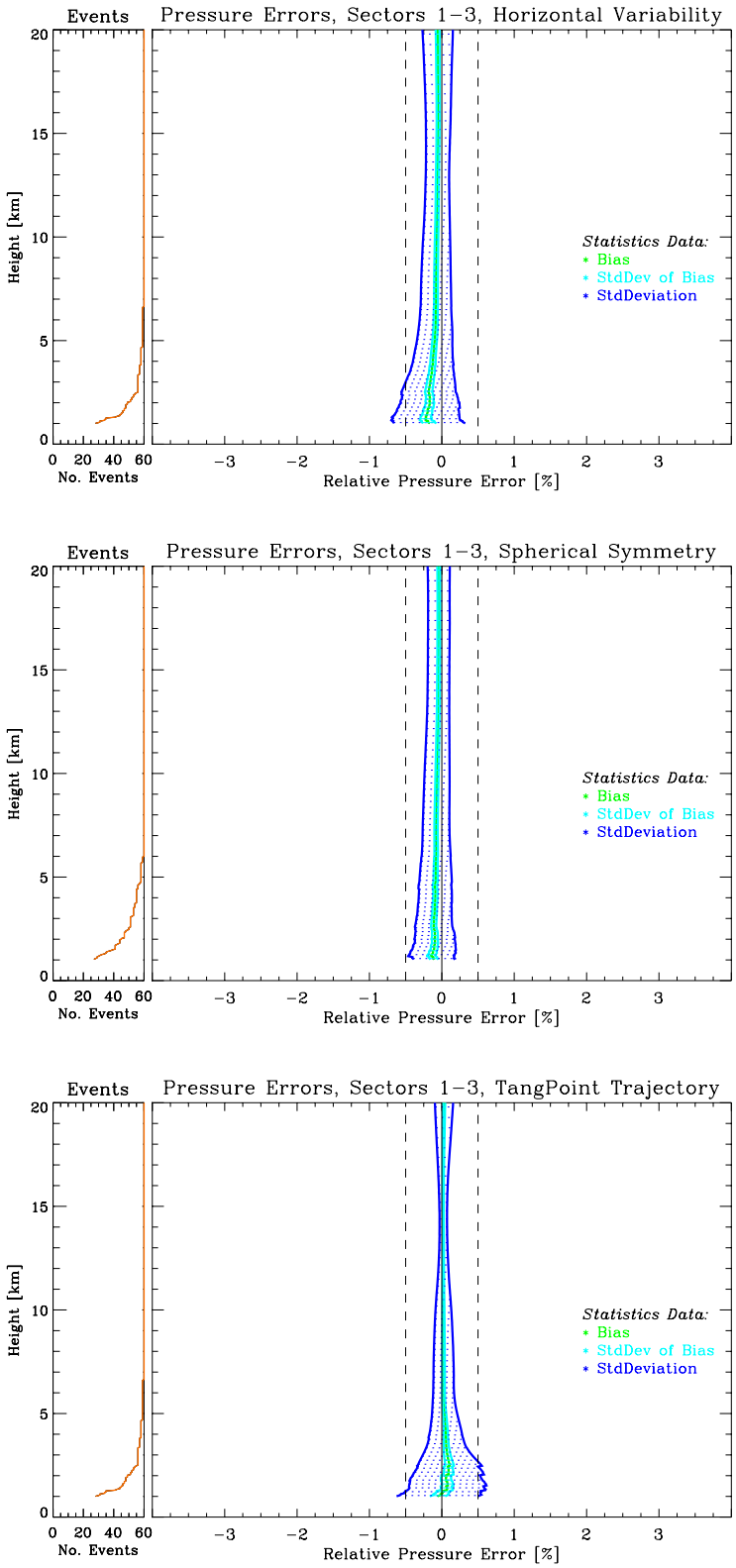

Fig. 5. Pressure error statistics for the ensemble of all 60 occultation events in all sectors. Top panel: atmosphere with horizontal variability; middle panel: atmosphere with spherical symmetry applied; bottom panel: difference vertical profile at mean tangent point–minus–along 3D tangent point trajectory.

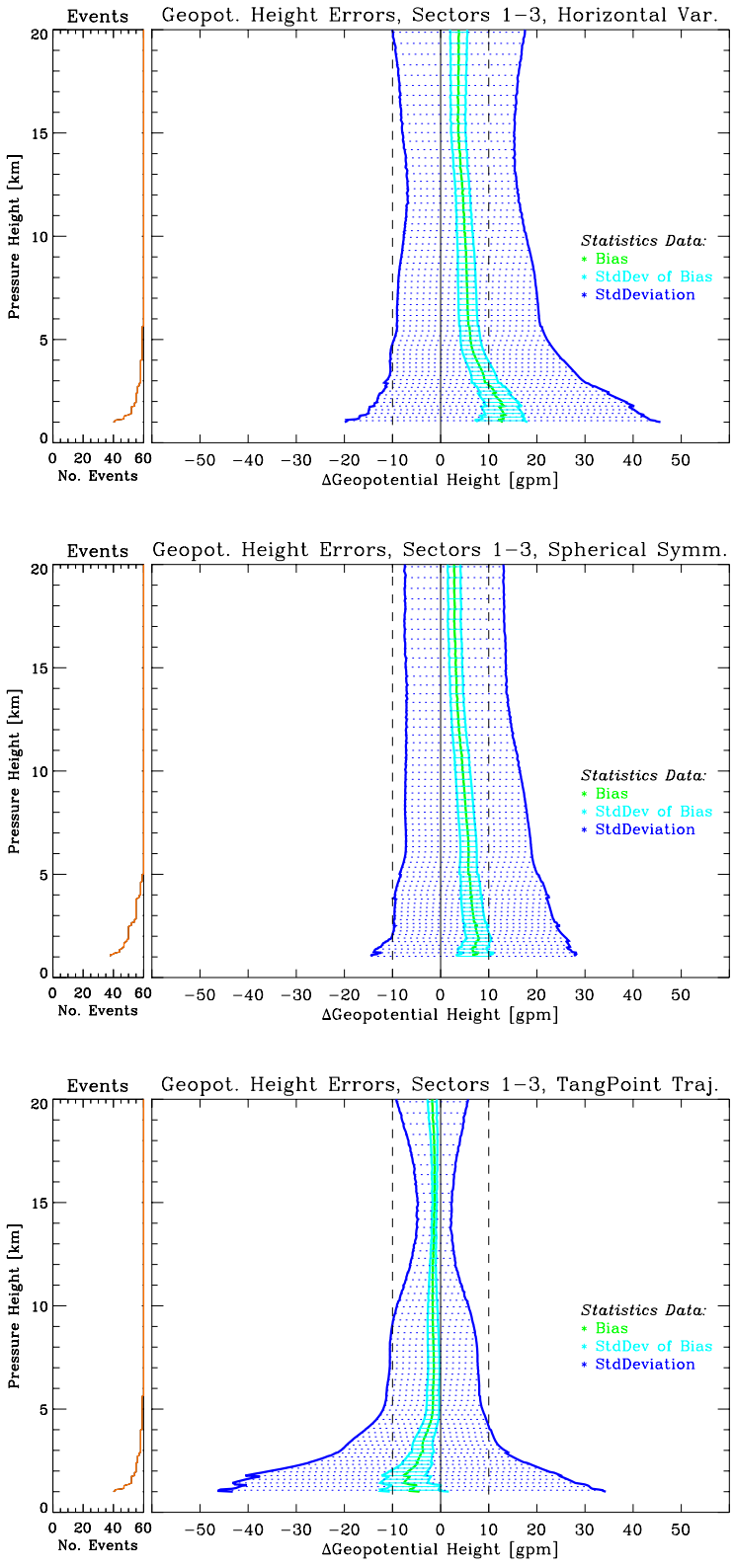

Fig. 6. Geopotential height error statistics for the ensemble of all 60 occultation events in all sectors. Top panel: atmosphere with horizontal variability; middle panel: atmosphere with spherical symmetry applied; bottom panel: difference vertical profile at mean tangent point–minus–along 3D tangent point trajectory.

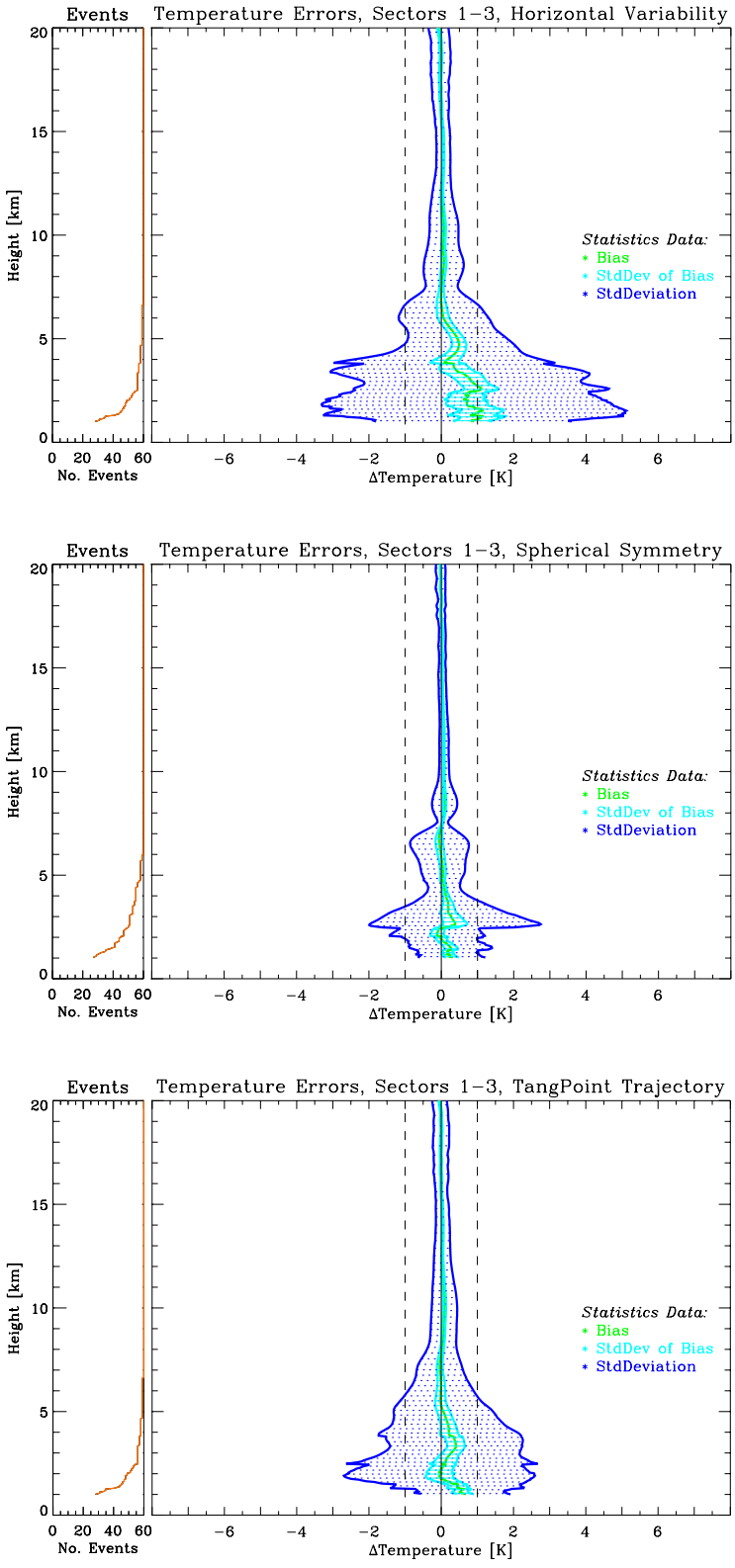

Fig. 7. Temperature error statistics for the ensemble of 60 all occultation events in all sectors. Top panel: atmosphere with horizontal variability; middle panel: atmosphere with spherical symmetry applied; bottom panel: difference vertical profile at mean tangent point–minus–along 3D tangent point trajectory.

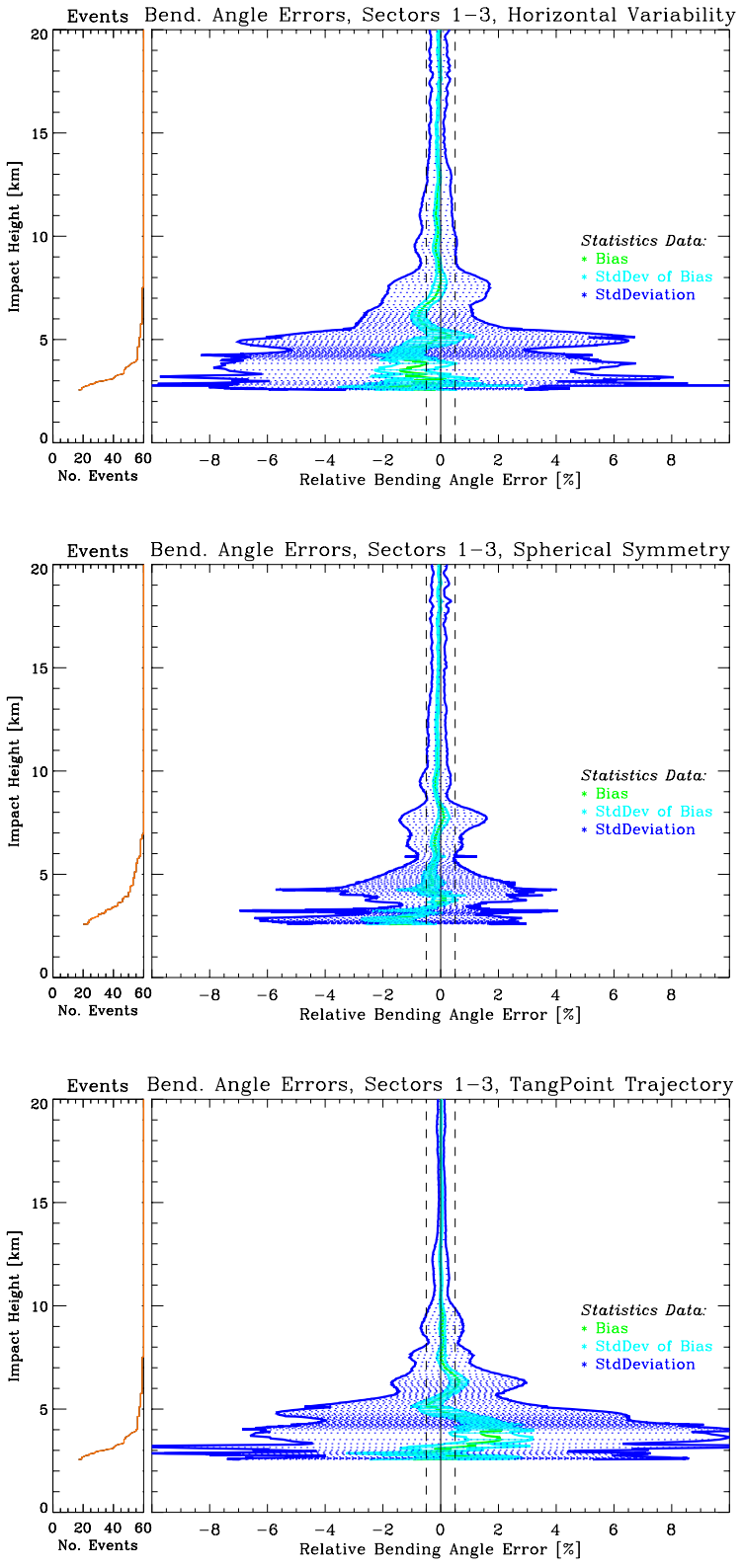

Fig. 8. Bending angle error statistics for the ensemble of 60 all occultation events in all sectors. Top panel: atmosphere with horizontal variability; middle panel: atmosphere with spherical symmetry applied; bottom panel: difference vertical profile at mean tangent point–minus–along 3D tangent point trajectory.

4. Sensitivity to the Angle-of-Incidence

In this part of the study, the sensitivity of retrieval products to the angle-of-incidence of occultation rays relative to the boresight direction of the receiving antenna (aligned with the LEO orbit plane) is analysed. Error analyses have been performed for each azimuth sector (ensembles of 20 events), for every atmospheric parameter under study.

Errors in refractivity, pressure, and bending angle, respectively, are – as in section 3 – displayed as relative values in units [%], geopotential height and dry temperature errors as absolute values in units [gpm] and [K], respectively. All statistics are shown between 1 km and 20 km above the (ellipsoidal) surface; the dashed vertical lines indicate relative errors of 0.5 % and absolute errors of 10 gpm and 1 K, respectively.

Each of the following figures, Figures 9 to 13, shows the results for sector 1 in the top panel, for sector 2 in the middle panel, and for sector 3 in the bottom panel, respectively (the three sectors are defined as described in section 2.1). Refractivity errors are shown in Figure 9, pressure errors in Figure 10, geopotential height errors in Figure 11, dry temperature errors in Figure 12, and bending angle errors in Figure 13, respectively.

One general result pertains to all parameters studied: Above ~5 to 10 km, the behavior of the result profiles for all parameters is quite similar in that errors increase with increasing angle-of-incidence. Below these heights this is only valid with several exceptions, which deserve further investigation. Also the relevance of reference profile geometry (as discussed in section 3.2) at different angles of incidence is worth to be inspected more closely in future work.

4.1. Refractivity Errors

The ensemble of 20 events with small angles-of-incidence (sector 1) has no significant bias (less than 0.1%) above 10 km height. Standard deviations in the same height interval are smaller than 0.2 %. Between 10 km and 2.5 km, bias and standard deviation increase almost continuously (with decreasing height) to 0.7% and 1.1%, respectively. Below ~2.5 km, the behavior is less uniform: the bias oscillates around ~0.6%, the standard deviation reaches maximum values of ~2% at ~1.3 km.

Events in sector 2 show remarkable features in the height interval below 10 km: The bias is explicitly smaller than in sector 1, while standard deviations are of comparable size (maximum: ~2.3% near 3.5 km). At 4.5 km, the bias reaches a maximum (negative) value of –0.3%, below that it oscillates around zero. Below 3.5 km, the error estimates become smaller again, which may partly root in the fact that the sample size decreases gradually (see left-hand-side subpanel of middle panel of Figure 9) leaving a smaller ensemble tendatively composed of more "well-behaved" profiles.

Events with angles-of-incidence between 40° and 50° (sector 3) exhibit an approximately constant negative bias of about 0.1% above 8 km height, while standard deviations are markedly larger. The largest biases (near 1%) and standard deviations (~2.5%) are encountered at around 1.5 to 2 km height.

4.2. Pressure Errors

All sectors display (generally very small) negative biases over the entire height domain. Standard deviation are smaller than 0.5 % almost everywhere; they are smallest in sector 1, whereas biases are smallest in sector 2.

Events in sector 1 exhibit biases of less than 0.1 % between 6 and 20 km, which are, nevertheless, slightly larger than corresponding biases in sector 2. Below 6 km, they gradually increase to ~0.25% at lowest levels. Standard deviations remain smaller than 0.4% at all heights.

Events in sector 2 have the smallest biases in the entire height domain: they are always smaller than ~0.1%. Standard deviations remain almost constant (about 0.15%) down to about 10 km, then they start to increase gradually but never exceed 0.5%.

Events in sector 3 display a marked (constant) negative bias of ~0.1% between 5 and 20 km height, while standard deviations amount to about 0.25% (approximately constant as well). Below 5 km, the bias increases continuously to ~0.35%. Standard deviation increase to ~0.55% at lowest levels.

4.3. Geopotential Height Errors

Geopotential height errors are, as already in Figure 4 of section 3, displayed as functions of pressure height. Positive biases (related to negative pressure biases) can be detected in all sectors. In line with the pressure error results they are smallest in sector 2, while standard deviations are smallest in sector 1.

The bias in sector 1 increases continuously from ~1.5 gpm at 20 km to 16 gpm at 1 km pressure height, the standard deviations from ~7.5 to ~20 gpm.

Sector 2 has again the smallest bias, the maximum is slightly more than 8 gpm near 2.5 km. Standard deviations grow evenly from ~10 gpm at 20 km to ~33 gpm at 1 km.

In sector 3 there is a pronounced positive bias of about 8 gpm between 20 km and 4 km, which increases downwards to about 25 gpm. Standard deviations rise from about 20 gpm at 20 km to about 40 gpm at 1 km.

4.4. Temperature Errors

The temperature errors (Figure 12) closely reflect the overall behavior of the refractivity errors (Figure 9), though with a change in sign leading to mirror-symmetry of temperature vs. refractivity errors. This behavior is caused by the inverse relation of the two parameters via the equation of state and was explored in detail by Rieder and Kirchengast (2001a; 2001b).

Events in sector 1 exhibit very small biases of less than ~0.1 K above 10 km, which slowly (but not uniformly) increase to 0.4 K at 4 km and come close to 2 K at lowest levels. Standard deviations increase from ~0.15 K at 20 km to ~2. 5 K at near 3 km.

Events in sector 2 are practically bias-free between 6 km and 20 km (biases < 0.1 K). Below this height, biases oscillate around zero but remain < 0.8 K throughout. Standard deviations in this lower height domain are only slightly larger than in sector 1.

Events in sector 3, finally, show small biases, never exceeding 0.1 K, down to about 9 km. Below 4 km, biases increase markedly and reach a maximum value of close to 2 K at 2.5 km. Standard deviations are around 0.5 K down to 10 km. Below 4 km, there is a pronounced increase of up to ~6 K between 1.5 and 2 km height.

4.5. Bending Angle Errors

The bending angle errors as function of impact height (Figure 13) are directly akin in their major characteristics to those in refractivity (Figure 9), though exhibiting higher relative error magnitude due to being, as explained in section 3.6, less smoothed than refractivity errors. As also mentioned in section 3.6, the estimated error magnitudes are presumably somewhat too conservative because reference bending angles were derived under spherical symmetry assumptions instead of employing rigorous 3D ray tracing.

Both in sector 1 and sector 2 biases are very small in the lower stratosphere (< 0.2%), in sector 2 even down to about 7 km, while they increase to values of about 2% in the lower troposphere. Standard deviations remain within 0.5% down to about 8 km in both sectors, while they increase to significantly larger values below and reach up to 10% at a few levels near 3 km in sector 1 and near 5 km in sector 2, respectively.

In sector 3, the bias also remains quite small down to ~10 km (< 0.25%) but increases, via some oscillations, to about 3% in the lower troposphere. The standard deviations start to exceed 0.5% at about 12 km and amount to around 2% between 5 and 8 km; below 5 km they also touch the 10% magnitude at a few levels.

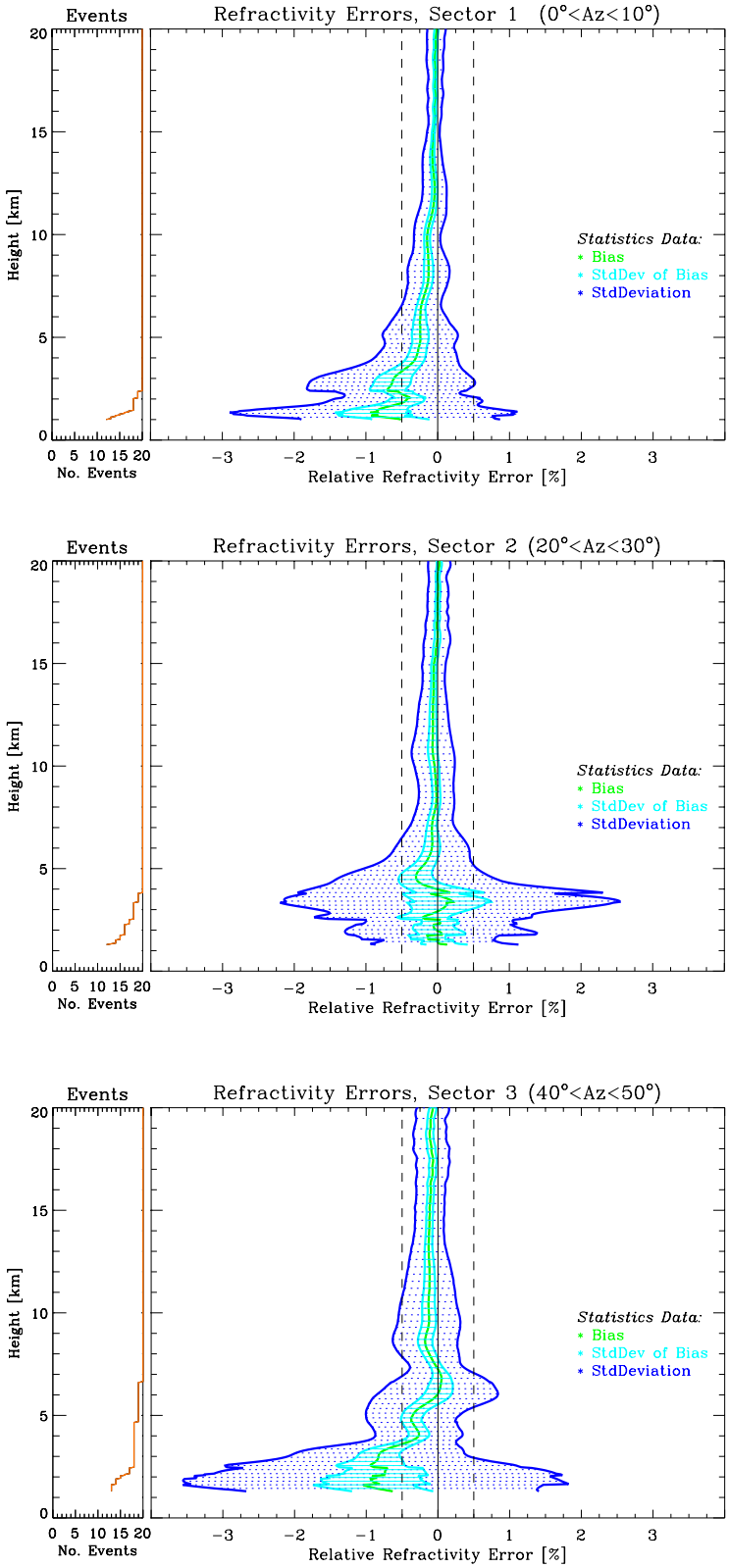

Fig. 9. Refractivity error statistics for occultation events in sector 1 (top panel), sector 2 (mid panel), and sector 3 (bottom panel), respectively.

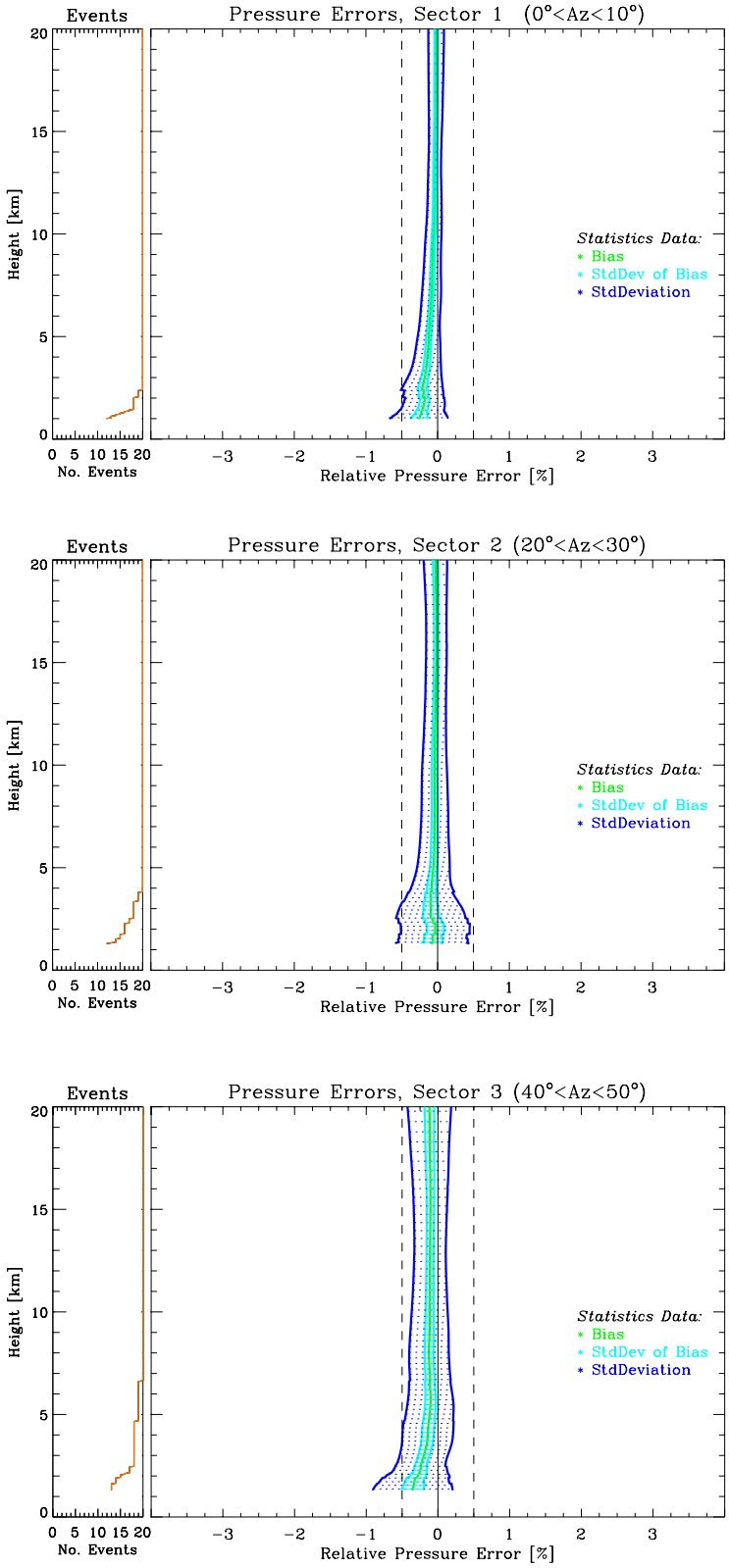

Fig. 10. Pressure error statistics for occultation events in sector 1 (top panel), sector 2 (mid panel), and sector 3 (bottom panel), respectively.

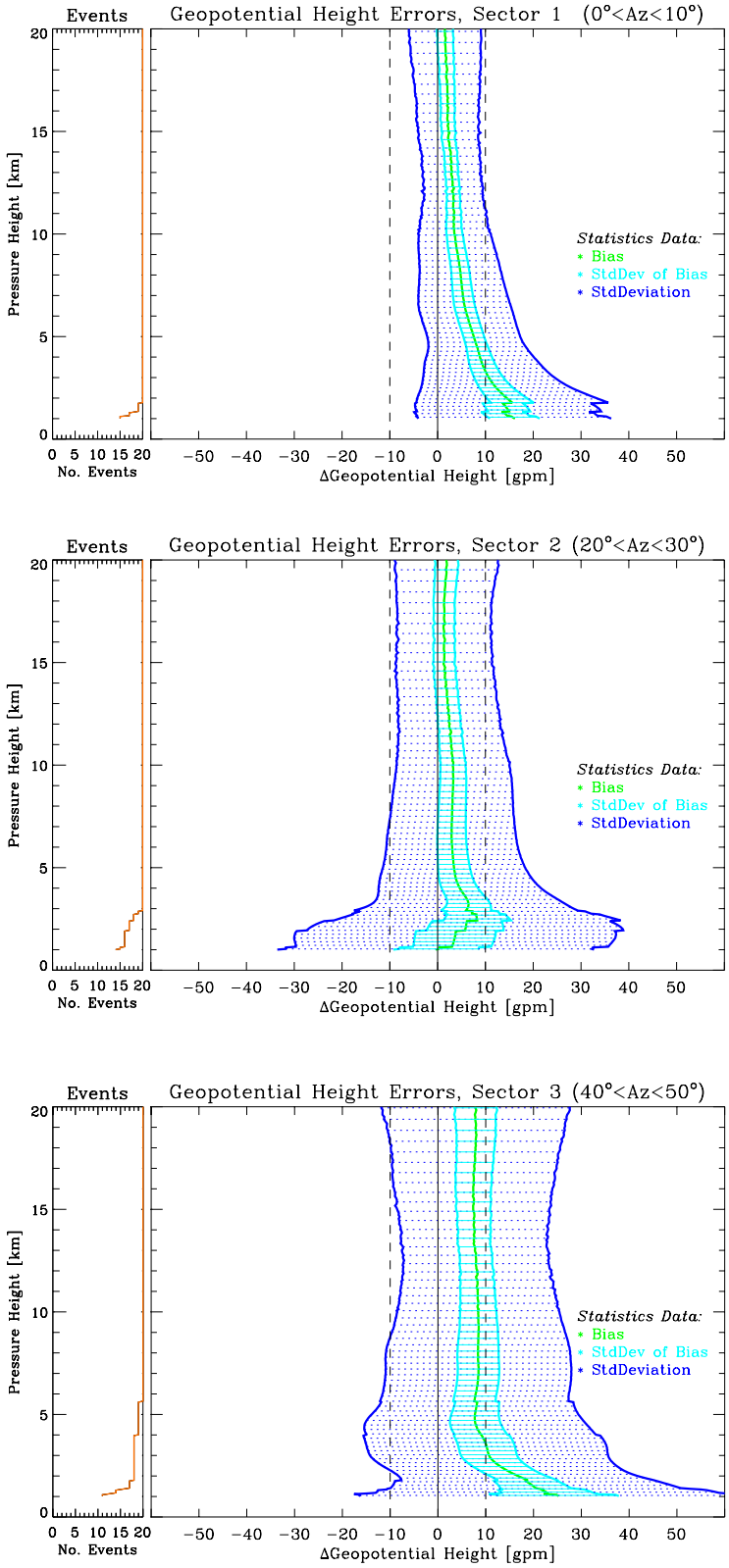

Fig. 11. Geopotential height error statistics for occultation events in sector 1 (top panel), sector 2 (mid panel), and sector 3 (bottom panel), respectively.

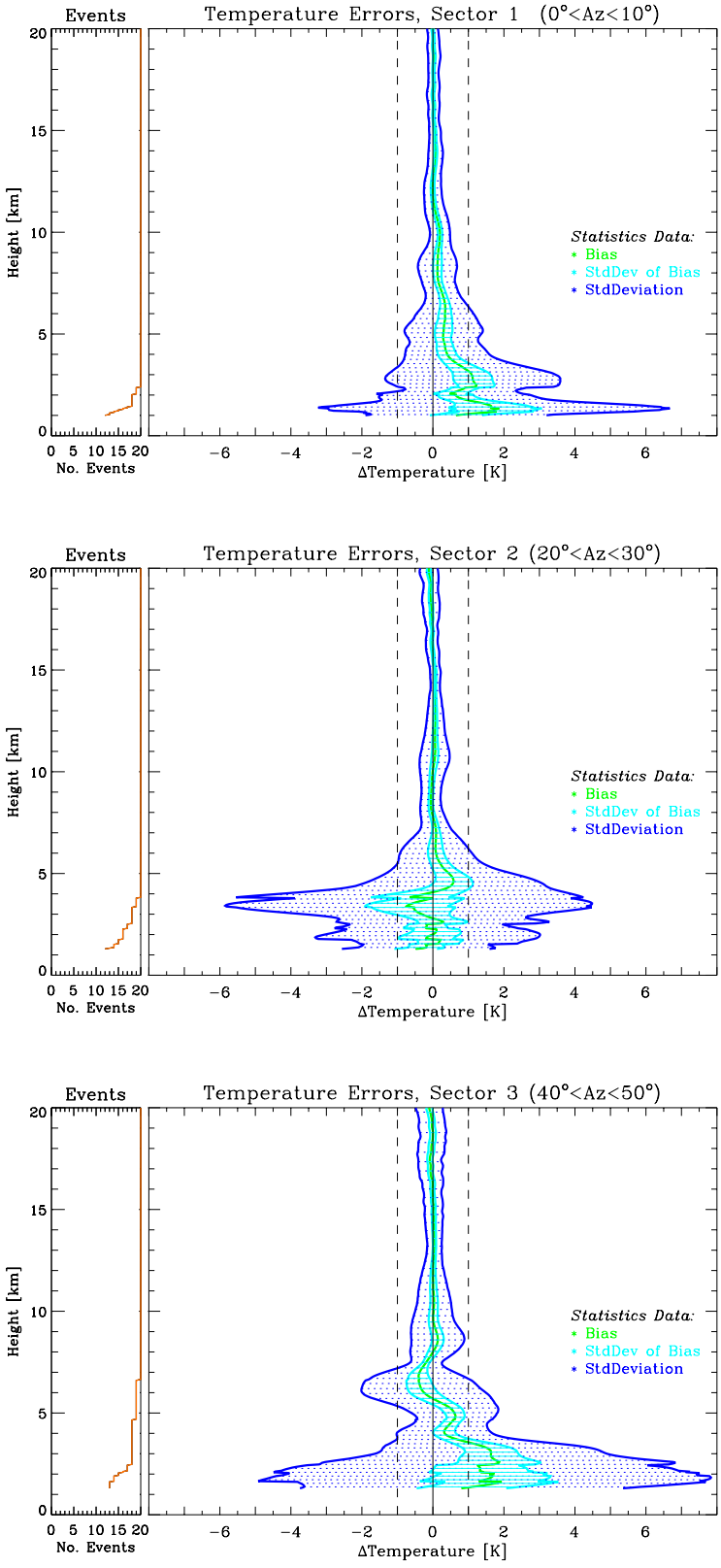

Fig. 12. Temperature error statistics for occultation events in sector 1 (top panel), sector 2 (mid panel), and sector 3 (bottom panel), respectively.

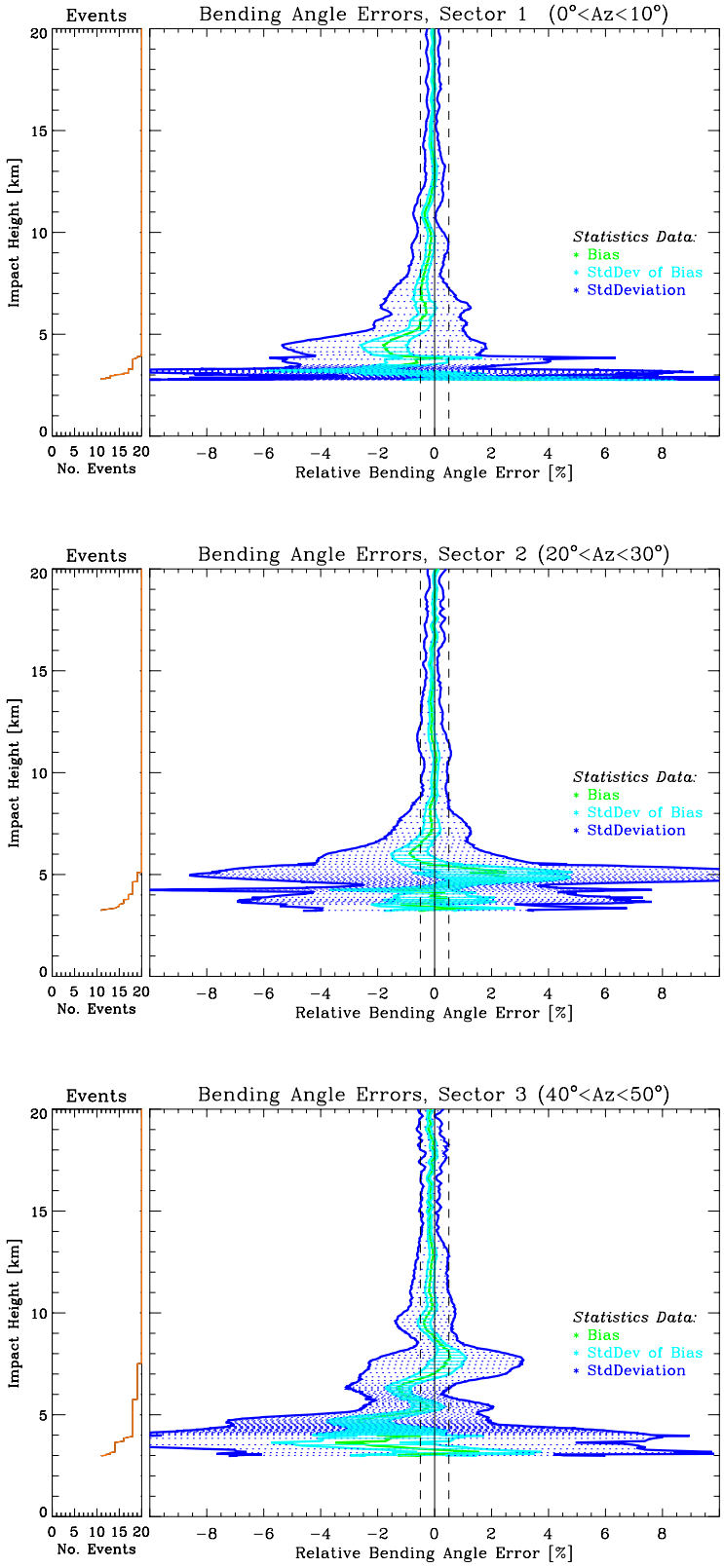

Fig. 13. Bending angle error statistics for occultation events in sector 1 (top panel), sector 2 (mid panel), and sector 3 (bottom panel), respectively.

5. Summary, Conclusions, and Outlook

This study addressed the sensitivity of GNSS radio occultation measurements to atmospheric horizontal variability errors.

First, the error of a realistic horizontally variable atmosphere relative to a spherically symmetric atmosphere was quantified based on an ensemble of 60 occultation events. This investigation was based on using a representative ECMWF T213L50 analysis field with and without horizontal variability, respectively. The relevance of either assuming the "true" profile vertically at a mean event location (the common practice) or more precisely along the 3D tangent point trajectory traced out during the event was assessed in this context as well.

Second, the sensitivity of retrieval products to the angle-of-incidence of occultation rays relative to the boresight direction of the receiving antenna was analyzed for three different azimuth sectors (0–10 deg, 20–30 deg, 40–50 deg; ensemble of 20 events in each sector).

All retrieved geophysical parameters of interest from bending angle via refractivity, pressure, and geopotential height to dry temperature have been investigated. The main results, and indications obtained on aspects deserving closer investigation in the future, can be summarized as follows.

Sensitivity to horizontal variability

Biases and standard deviations of the considered atmospheric parameters under spherical symmetry are significantly smaller than corresponding errors in a realistic atmosphere with horizontal variability. The differences are most pronounced below ~7 km height.

Temperature standard deviations below 5 km, for example, remain smaller than 2.5 K in a spherically symmetric atmosphere while they reach values of about 4 K in the realistic atmosphere. This behavior confirms the prominent role – as for example found earlier by Kursinki *et al.* (1997) under more simplified conditions – horizontal variability plays as an error source in the troposphere.

Dry temperature profiles between 7 km and 20 km were found to be essentially bias-free in both the realistic and spherical-symmetry scenarios (biases smaller than 0.1 K), which confirms the unique climate monitoring utility of GNSS occultation data. Small residual biases of ~0.2–0.3 K between about 7 km and 14 km where found, though, for ensembles of events at high latitudes within separate parallel work (Foelsche et al., 2001; Steiner and Kirchengast, unpubl. manuscript, 2002; Kirchengast et al., unpubl. manuscript, 2002). Within this study, involving only about 10 events at high latitudes (poleward of 60 deg), that residual bias was (partly) visible only in the results for the 0–10 deg azimuth sector. Nevertheless, it certainly calls for closer study in the future.

A significant part of the total error below ~7 km can be attributed to adopting refererence profiles vertically at mean tangent point locations (designed to fit best at heights around 15 km) instead of extracting them along actual 3D tangent point trajectories through the troposphere. This finding indicates the importance of utilizing tropospheric RO profiles not just vertically but as good as possible consistent with the actual tangent point trajectory (or, more generally, occultation plane movement). Future work will investigate this matter more closely based on an even higher-resolved field (ECMWF T511L60 analysis field) and will also rigorously inspect by how much the standard deviation and bias errors decrease if the data

are exploited along a tangent point trajectory deduced purely from observed data, mainly GNSS and LEO satellite position and bending angle data.

Sensitivity to angle-of-incidence

Below about 7 km, the general result for all parameters studied is qualitatively quite clear: most errors were found to increase with increasing angle of incidence. This is in line with the hypothesis that larger angles of incidence lead to more sensitivity to horizontal variability.

Biases in the 20–30 deg azimuth sector are generally smaller than corresponding biases in the 0–10 deg sector, however, despite the latter is associated with almost co-planar GNSS and LEO satellites, which should lead to the most-vertical and best-quality occultation events. That the biases apparently to not concur with this expectation merits further investigation.

In general, the sensitivity of bias errors to increases of the angle of incidence has been found to be relatively small, which is favorable regarding the climate monitoring utility of the data. For example, dry temperature biases between 7 km and 20 km exhibit no relevant increase with increasing angle of incidence. Current cautionary approaches restricting the events used in climate studies to small angles of incidence (such as < 15 deg; Steiner et al., 2001) may thus be overly conservative.

Future work, in a first step, needs to further improve the understanding of all errors involved, in particular of the residual biases, in order to eliminate or mitigate them to the largest extend possible in a second step. This will optimize the climatological quality of the data at all angles of incidence.

Acknowledgments. The authors thank A.K. Steiner (IGAM/UG) and S. Syndergaard (Univ. of Arizona, Tucson, U.S.A.) for support in preparing some auxiliary computer codes used in the study, in particular the forward Abel transform. The EGOPS software, the core tool of the study, was developed by an international consortium led by IGAM/UG and involving partner teams at Danish Meteorological Institute and TERMA Elektronik A/S, Denmark, the Met. Office, U.K., and Austrian Aerospace GmbH, Austria, with the major funding provided by the European Space Agency. The European Centre for Medium-Range Weather Forecasts (ECMWF, Reading, U.K.) provided the atmospheric analysis field used. The study was funded by the European Space Agency under ESA/ESTEC Contract No. 14809/00/NL/MM. Furthermore, U.F. received financial support for the work from the START research award of G.K. funded by the Austrian Ministry for Education, Science, and Culture and managed under Program No. Y103-CHE of the Austrian Science Fund.

References

Gobiet, A., and G. Kirchengast, Sensitivity of atmospheric profiles retrieved from GNSS occultation data to ionospheric residual and high-altitude initialization errors, *Techn. Report for ESA/ESTEC No. 1/2002*, Inst. for Geophys., Astrophys., and Meteorol., Univ. of Graz, Austria, 2002.

Gorbunov, M.E., Radioholographic methods for processing radio occultation data in multi-path regions, *DMI Tech. Report 01-02*, Danish Met. Inst., Copenhagen, Denmark, 2001a.

Gorbunov, M.E., Radio-holographic analysis and validation of Mircrolab-1 radio occultation data in the lower troposphere, *J. Geophys. Res.*, submitted manuscript, 2001b.

GRAS-SAG, The GRAS instrument on METOP, *ESA/EUMETSAT Rep. (ESA No. VR/3021 /PI, EUM.No. EPS/MIS/IN/9)*, 38 pp., ESA/ESTEC, Noordwijk, Netherlands, 1998.

Foelsche, U., G. Kirchengast, A.K. Steiner, L. Kornblueh, E. Manzini, and L. Bengtsson, Klimawandel-Monitoring mit satellitengetragenen GNSS Okkultationssensoren, *Proc. CD-Rom DACH (deutsch-österr.-schweiz.) Meteorologentagung 2001,* Sept. 2001, Vienna, Austria, 19p., 2001.

Healy, S.B., and J.R. Eyre, Retrieving temperature, water vapour and surface pressure information from refractive-index profiles derived by radio occultation: A simulation study, *Quart. J. Roy. Meteorol. Soc.*, 126, 1661-1683, 2000.

Hedin, A.E., Extension of the MSIS thermosphere model into the middle and lower atmosphere, *J. Geophys. Res.*, 96, 1159-1172, 1991.

Hoeg, P., A.S. Jensen, H. Vedel, E. Kaas, and G. Kirchengast, ACE (Atmosphere Climate Experiment) Scientific Support Study, *Proposal to ESA/ESTEC*, 40p., Danish Met. Institute, Copenhagen, Denmark, 2000.

Kirchengast, G., End-to-end GNSS Occultation Performance Simulator overview and exemplary applications, *Wissenschaftl. Ber. No. 2/1998*, Inst. for Meteorol. and Geophys., Univ. of Graz, Austria, 1998.

Kirchengast, G., J. Fritzer, and J. Ramsauer, End-to-end GNSS Occultation Performance Simulator Version 4 (EGOPS4) Software User Manual (Overview and Reference Manual), *Techn. Report for ESA/ESTEC No. 5/2001*, Inst. for Geophys., Astrophys., and Meteorol., Univ. of Graz, Austria, 2001.

Kursinski, E.R., G.A. Hajj, J.T. Schofield, R.P. Linfield, and K.R. Hardy, Observing earth's atmosphere with radio occultation measurements using the Global Positioning System, *J. Geophys. Res.*, 102, D19, 23429 - 23465, 1997.

Landolt-Börnstein, *Geophysics of the Solid Earth, the Moon and the Planets – Numerical Data and Functional Relationships in Science and Technology,* Vol. V/2a (Fuchs, K., and H. Stoffel, Eds.), 332–336, Springer Verlag, Berlin–Heidelberg, 1984.

Rieder, M.J., and G. Kirchengast, Error analysis for mesospheric temperature profiling by absorptive occultation sensors, *Ann. Geophys.*, 19, 71–81, 2001a.

Rieder, M.J., and G. Kirchengast, Error analysis and characterization of atmospheric profiles retrieved from GNSS occultation data, *J. Geophys. Res.*, 106, 31,755–31,770, 2001b.

Salby, M.L., *Fundamentals of Atmospheric Physics,* Academic Press, San Diego, 1996.

Smith, E.K., and S. Weintraub, The constants in the equation for atmospheric refractive index at radio frequencies, *Proceedings of the I.R.E.,* 41, 1035-1037, 1953.

Steiner, A.K., G. Kirchengast, and H.P. Ladreiter, Inversion, error analysis and validation of GPS/MET occultation data, *Ann. Geophysicae*, 17, 122-138, 1999.

Steiner, A.K., G. Kirchengast, U. Foelsche, L. Kornblueh, E. Manzini, and L. Bengtsson, GNSS occultation sounding for climate monitoring, *Phys. Chem. Earth (A),* 26, 113–124, 2001.

Syndergaard, S., Retrieval analysis and methodologies in atmospheric limb sounding using the GNSS radio occultation technique. *DMI Scient. Report 99-6*, 131 pp., Danish Meteorol. Institute, Copenhagen, Denmark, 1999.

Appendix A.

A.1. Satellite two line element (TLE) files

METOP satellite

```
METOP-1                   M1
1     1  99212USR 99212.50000000  .00000000  00000-0  00000-0 0  0010
2     1  98.7047 264.3857 0011650  90.0000 294.1230 14.21635855     0
```

GPS satellites

```
GPS BII-01  (PRN 14)      E1/STD OP
1 19802U 89013A   99211.02056368 -.00000020  00000-0  00000+0 0  2647
2 19802  55.3439 108.9711 0019265 168.3663 191.5954  2.00549436 54550
GPS BII-02  (PRN 02)      B3/STD OP
1 20061U 89044A   99207.37758610  .00000064  00000-0  10000-3 0  2464
2 20061  54.1998 284.8446 0159014 220.6796 138.1554  2.00562746 52247
GPS BII-04  (PRN 19)      A4/STD OP
1 20302U 89085A   99211.23953477  .00000064  00000-0  10000-3 0  2577
2 20302  53.2388 224.4672 0032129 191.5461 168.4294  2.00567430 49676
GPS BII-05  (PRN 17)      D3/STD OP
1 20361U 89097A   99211.75201330 -.00000025  00000-0  10000-3 0  1012
2 20361  56.0230  51.5905 0087567 133.7643 227.0406  2.00565375 39168
GPS BII-06  (PRN 18)      F3/STD OP
1 20452U 90008A   99210.15164647  .00000016  00000-0  10000-3 0  1962
2 20452  54.0437 165.0892 0060382  88.6501 272.0071  2.00572412 47638
GPS BII-07  (PRN 20)      B2/STD NA
1 20533U 90025A   99212.55144824 -.00000013  00000-0  00000+0 0  2382
2 20533  54.5433 285.3567 0050958  77.2727 283.3724  2.00568969 46457
GPS BII-08  (PRN 21)      E2/STD OP
1 20724U 90068A   99209.88125894 -.00000026  00000-0  00000+0 0   842
2 20724  54.9707 107.0253 0133933 168.1072 191.4174  2.00564969 42266
GPS BII-09  (PRN 15)      D2/STD OP
1 20830U 90088A   99209.93647457 -.00000020  00000-0  00000+0 0   598
2 20830  55.9845  49.6188 0068048  95.4629 265.3777  2.00565458 42905
GPS BIIA-10 (PRN 23)      E4/STD OP
1 20959U 90103A   99212.82735991 -.00000013  00000-0  10000-3 0   341
2 20959  55.1677 108.9809 0112424 234.1838 124.8163  2.00557011 41557
GPS BIIA-11 (PRN 24)      D1/STD OP
1 21552U 91047A   99210.10957741 -.00000020  00000-0  10000-6 0  9954
2 21552  56.2576  47.4052 0071446 247.9064 111.3985  2.00563232 37094
GPS BIIA-12 (PRN 25)      A2/STD OP
1 21890U 92009A   99211.06870246  .00000068  00000-0  00000+0 0  8297
2 21890  53.7865 224.9316 0048203 257.5396 101.7509  2.00571281 32483
GPS BIIA-14 (PRN 26)      F2/STD OP
1 22014U 92039A   99210.32068005  .00000018  00000-0  00000+0 0  7462
2 22014  54.8518 166.9368 0094691 327.3406  32.0303  2.00574839 23234
GPS BIIA-15 (PRN 27)      A3/STD OP
1 22108U 92058A   99210.28472674  .00000078  00000-0  10000-3 0  7655
2 22108  54.0170 225.8063 0121675 163.4095 197.0188  2.00564714 28416
GPS BIIA-16 (PRN 01)      F1/STD OP
1 22231U 92079A   99210.96480552  .00000015  00000-0  00000+0 0  7616
2 22231  54.6764 168.0573 0038326 269.5681  89.9905  2.00570063 27005
GPS BIIA-17 (PRN 29)      F4/STD OP
1 22275U 92089A   99212.08946777  .00000007  00000-0  00000+0 0  7617
2 22275  54.6341 165.4993 0065894 243.3264 116.0806  2.00583533 26432
GPS BIIA-18 (PRN 22)      B1/STD OP
1 22446U 93007A   99213.17842250 -.00000018  00000-0  00000+0 0  7512
```

```
2 22446  54.1885 285.4429 0093963  51.5078 309.4033  2.00549297 25446
GPS BIIA-19 (PRN 31)      C3/STD OP
1 22581U 93017A   99205.34147734 -.00000059  00000-0  10000-3 0  5594
2 22581  55.2367 346.5691 0071130  47.7086 312.8939  2.00559492 24340
GPS BIIA-20 (PRN 07)      C4/STD OP
1 22657U 93032A   99212.45593958 -.00000080  00000-0  10000-3 0  6818
2 22657  55.2237 346.1492 0081583 222.1335 137.2460  2.00569714 19816
GPS BIIA-21 (PRN 09)      A1/STD OP
1 22700U 93042A   99208.43184636  .00000090  00000-0  10000-3 0  5741
2 22700  54.1813 226.7170 0049438 357.8627   2.1765  2.00558214 22536
GPS BIIA-22 (PRN 05)      B4/STD OP
1 22779U 93054A   99210.01409292 -.00000010  00000-0  10000-3 0  6345
2 22779  54.3403 285.6223 0016281 264.1972  95.6871  2.00575626 21322
GPS BIIA-23 (PRN 04)      D4/STD OP
1 22877U 93068A   99213.05733970 -.00000040  00000-0  10000-3 0  4429
2 22877  55.7080  47.4183 0039688 302.2128  57.3214  2.00574425 20274
GPS BIIA-24 (PRN 06)      C1/STD OP
1 23027U 94016A   99210.64396927 -.00000075  00000-0  10000-3 0  3865
2 23027  55.1214 348.1603 0066232 203.0143 156.6907  2.00557362 17531
GPS BIIA-25 (PRN 03)      C2/STD OP
1 23833U 96019A   99211.27815945 -.00000078  00000-0  00000+0 0   574
2 23833  54.6834 346.3371 0036864 149.3084 210.9108  2.00564351  2520
GPS BIIA-26 (PRN 10)      E3/STD NA
1 23953U 96041A   99213.18975446 -.00000014  00000-0  00000+0 0   117
2 23953  55.0399 106.5549 0016030 324.3023  35.6476  2.00577860   367
```

A.2. Mission Analysis/Planning

```
[*** MAnPl Input File for Task M19990915_bore135 ***]

-----------------------------------------------------------------------
[*Project-Id and Task-Id*]
Project-Id               = ACESS
Task-Id                  = M19990915_bore135
-----------------------------------------------------------------------

[*Data Type Selection*]
Data Type                = Occultation Data

[*UT Range*]
Start_Time               = 990915.000000  [yymmdd.hhmmss]
Simul_Time_Range         = 0240000        [hhhmmss]

[*Height Levels*]
Hlo1 Hhi1 HStep1 dh1     =    0.0  10.0   2.0  0.20  [km]
Hlo2 Hhi2 HStep2 dh2     =   20.0  90.0  10.0  1.00  [km]

[*Geographic Area of Interest for Occultation Events*]
GeogrAreaChoice          = Global

[*GNSS-LEO Ray Treatment*]
RayTreatmentChoice       = Bended Rays (Exp. Atmos.)

[*Earth Figure Model*]
EarthFigModelChoice      = Ellip.WGS84

[*GRAS Antennae Specifications*]
-V AntennnaChoice        = Used
-V BoresightElevation    =  27.0 [deg]
-V BoresightAzimuth      = 135.0 [deg]
-V FOVChoice             = Ell_Cartes
-V TPBW Vertical         =  90.0 [deg]
-V TPBW Horizontal       =  10.0 [deg]
+V AntennnaChoice        = Used
+V BoresightElevation    =  27.0 [deg]
+V BoresightAzimuth      =  45.0 [deg]
+V FOVChoice             = Ell_Cartes
+V TPBW Vertical         =  90.0 [deg]
+V TPBW Horizontal       =  10.0 [deg]

[*LEO Specifications*]
LEOOrbElemFilename       = leoMETOP1999212.tle
LEOOrbModelChoice        = SGP Orbits (Impr. Kepler)

[*GNSS Specifications*]
GPS SatSystemChoice      = Standard
GPSOrbElemFilename       = gps99212.tle
GLON SatSystemChoice     = None
GNSSOrbitModelChoice     = Keplerian Orbits

[*Visibility Infos on Differencing*]
DiffVisInfChoice         = No_Diff_Vis_info
TrackVisInfChoice        = No_Track_Vis_info

[*** EOF MAnPl Input File for Task M19990915_bore135 ***]
```

A.3. Forward Modeling

```
[*** FoMod Input File for Task F19990915_bore135_set ***]

-----------------------------------------------------------------
[*Project-Id and Task-Id*]
Project-Id              = ACESS
Task-Id                 = F19990915_bore135_set
-----------------------------------------------------------------

[*Occ. Event Simulation Type/Specifications*]
OccEventSimulType       = Sample of Events/Realistic Geometry
OccEv.HeightRange       =    0.0  90.0 [km]
ReferenceMAnPl/Task-Id  = M19990915_bore135_set
OccNoRange              =     1    5    1

[*Atmospheric Models Choice/Specifications*]
AtmClimModelChoice      = GCM 3D Atmosphere (GCM3DAtm)
GRIB Data FilePath      = /home/gcm/data/ozone/
GRIB Data FileName      = ecmwf19990915121.grb
Humidity Choice         = Humidity included (moist air)
AtmModelStructureChoice  = Sph. Symmetry (no horizontal var.) or, alternatively,
AtmModelStructureChoice = Atmos. Model Structure as is
AtmDistModelChoice      = No Atmos. Disturbance superposed

[*Ionospheric Models Choice/Specifications*]
IonClimModelChoice      = No Ionosphere
Sol.Act./F10.7 index    = n/a
IonModelStructureChoice = Ionos. Model Structure as is
IonDistModelChoice      = No Ionos. Disturbance superposed

[*Forward Modeling Sampling Rates*]
GPS Sampling Rates      =   10.0  10.0 [Hz]
GLON Sampling Rates     = No GLON Event

[*Signal Propagation Simulator Specifications*]
PropSimulatorType       = Full-3D Ray Tracer
PropSimulatorAccuracy   = <  ~1 mm

[*Earth Figure Model*]
EarthFigModelChoice     = Ellip.WGS84

[*GNSS-LEO Ray Treatment*]
RayTreatmentChoice      = Bended Rays (Exp. Atmos.)

[*GRAS Antennae Specifications*]
-V AntennnaChoice       = Used
-V BoresightElevation   =  27.0 [deg]
-V BoresightAzimuth     = 135.0 [deg]
-V FOVChoice            = Ell_Cartes
-V TPBW Vertical        =  90.0 [deg]
-V TPBW Horizontal      =  10.0 [deg]
+V AntennnaChoice       = Not used

[*LEO Specifications*]
LEOOrbElemFilename      = leoMETOP1999212.tle
LEOOrbModelChoice       = SGP Orbits (Impr. Kepler)

[*GNSS Specifications*]
GPS SatSystemChoice     = Standard
GPSOrbElemFilename      = gps99212.tle
GLON SatSystemChoice    = None
GNSSOrbitModelChoice    = Keplerian Orbits

[*** EOF FoMod Input File for Task F19990915_bore135_set ***]
```

A.4. Observation System Modeling

```
[*** OSMod Input File for Task O19990915_bore135_set ***]

-----------------------------------------------------------------------
[*Project-Id and Task-Id*]
Project-Id               = ACESS
Task-Id                  = O19990915_bore135_set
-----------------------------------------------------------------------

[*Occ. Event Simulation Type/Specifications*]
OccEventSimulType        = Sample of Events/Realistic Geometry
OccEv.HeightRange        =    0.0  90.0 [km]
ReferenceFoMod/Task-Id   = F19990915_bore135_set
OccNoRange               =     1    5    1

[*Receiver Sampling Rates*]
GPS Sampling Rates       =   10.0  10.0 [Hz]
GLON Sampling Rates      = No GLON Event

[*Transmitter Signal Powers*]
L1-C/A L2-P GPS Powers   =  27.0 20.0 [dBW]
L1-C/A L2-P GLON Powers  = No GLON Event

[*POD Error Modeling/Specifications*]
PODErrorModelChoice      = Kinematic POD Error Model
ErrApplicationType       = As specfied
RadialPositionErrorGNSS  =   0.20 [m]
RadialPositionErrorLEOs  =   0.40 [m]
AlongRayVelocityError    =   0.05 [mm/s]
AlongRayAccelError       =   0.05 [µm/s²]

[*Receiving System Simulator Specifications*]
Rec. Sys. Simulator      = Parameterized Receiving System Simulator

[*GRAS Antennae Modeling*]
-V AntennnaChoice        = Used
-V BoresightElevation    =  27.0 [deg]
-V BoresightAzimuth      = 135.0 [deg]
-V FOVChoice             = Ell_Cartes
-V HPBW Vertical         =  90.0 [deg]
-V HPBW Horizontal       =  10.0 [deg]
-V AntennaGain/Boresight =  11.0 [dB]
+V AntennnaChoice        = Not used

[*Receiver Performance Modeling*]
RecPerfModelChoice       = Realistic Perf./Noise Model
LoopBandwidth/singleside =  10.0 [Hz]
LEOAntennaeNoiseTemp     = 150.0 [K]
QuantLevelsADConversion  =   4

[*Local Multipath Modeling*]
LocalMultipModelChoice   = Sinusoidal Multipath Model
MultiPhaseErrPeriod      =   300.0    0.0    0.0    0.0 [sec]
MultiPhaseErrAmplitude   =   1.0  0.0  0.0  0.0  [mm]
MultiPhaseErrAmplTopRay  =   0.0  0.0  0.0  0.0  [mm]

[*Differencing Treatment/Clocks Modeling*]
DiffTreatmentChoice      = Groundb. Single Differencing
RelStabilityofWorstClock = 1.0E-13 [1secAllan]
AtmNoise per Groundlink  = 1.0E-13 [1secAllan]

[*Atmospheric Models Choice/Specifications*]
```

```
AtmClimModelChoice       = GCM 3D Atmosphere (GCM3DAtm)
GRIB Data FilePath       = /home/gcm/data/ozone/
GRIB Data FileName       = ecmwf19990915121.grb
Humidity Choice          = Humidity included (moist air)
AtmModelStructureChoice  = Atmos. Model Structure as is
AtmDistModelChoice       = No Atmos. Disturbance superposed

[*Ionospheric Models Choice/Specifications*]
IonClimModelChoice       = No Ionosphere
Sol.Act./F10.7 index     = n/a
IonModelStructureChoice  = Ionos. Model Structure as is
IonDistModelChoice       = No Ionos. Disturbance superposed

[*Earth Figure Model*]
EarthFigModelChoice      = Ellip.WGS84

[*** EOF OSMod Input File for Task O19990915_bore135_set ***]
```

A.5. Inversion/Retrieval

```
[*** InRet Input File for Task I19990915_bore135_set ***]

-----------------------------------------------------------------
[*Project-Id and Task-Id*]
Project-Id               = ACESS
Task-Id                  = I19990915_bore135_set
-----------------------------------------------------------------

[*Occ. Event Type/Specifications*]
OccDataType              = SimData
OccEventType             = Sample of Events/Realistic Geometry
OccNoRange               =     1    5    1
OccEv.HeightRange        =    0.0  90.0 [km]
ReferenceOSMod/Task-Id   = O19990915_bore135_ris

[*Bending Angle Retrieval Specifications*]
BendAngleRetToolChoice   = IAP Diff.Corr & Ion.Corr. & Bend.Angle Retrieval
DiffCorrectionType       = Canonical Transform

[*Refractivity Profiles Retrieval Specifications*]
RefProfRetToolChoice     = DMI Abel Transform Atmos.Refr.Profiles Retrieval

[*Atmospheric Profiles Retrieval Specifications*]
AtmProfRetToolChoice     = DMI Dry Air Prof. Retrieval

[*Atmospheric Models Choice/Specifications*]
AtmClimModelChoice       = GCM 3D Atmosphere (GCM3DAtm)
GRIB Data FilePath       = /home/gcm/data/ozone/
GRIB Data FileName       = ecmwf19990915121.grb
Humidity Choice          = Humidity included (moist air)
AtmModelStructureChoice  = Atmos. Model Structure as is
AtmDistModelChoice       = No Atmos. Disturbance superposed

[*Ionospheric Models Choice/Specifications*]
IonClimModelChoice       = No Ionosphere
Sol.Act./F10.7 index     = n/a
IonModelStructureChoice  = Ionos. Model Structure as is
IonDistModelChoice       = No Ionos. Disturbance superposed

[*Earth Figure Model*]
EarthFigModelChoice      = Ellip.WGS84

[*** EOF InRet Input File for Task I19990915_bore135_set ***]
```

Appendix B.

B.1. Dry Temperature Profiles, Horizontal Variability, Sector 1

Setting Events, Az = 170 – 180 deg

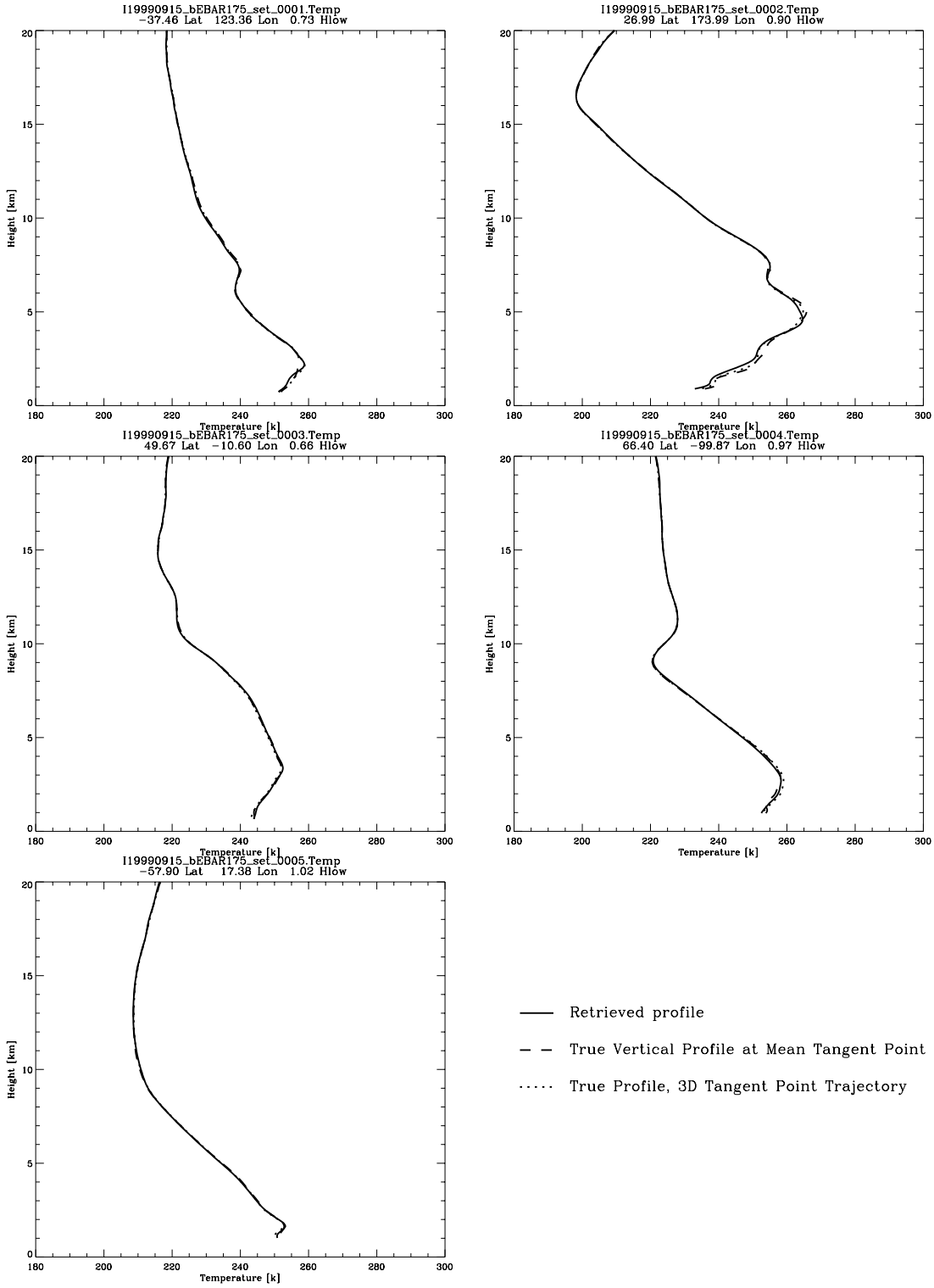

Setting Events, Az = 180 – 190 deg

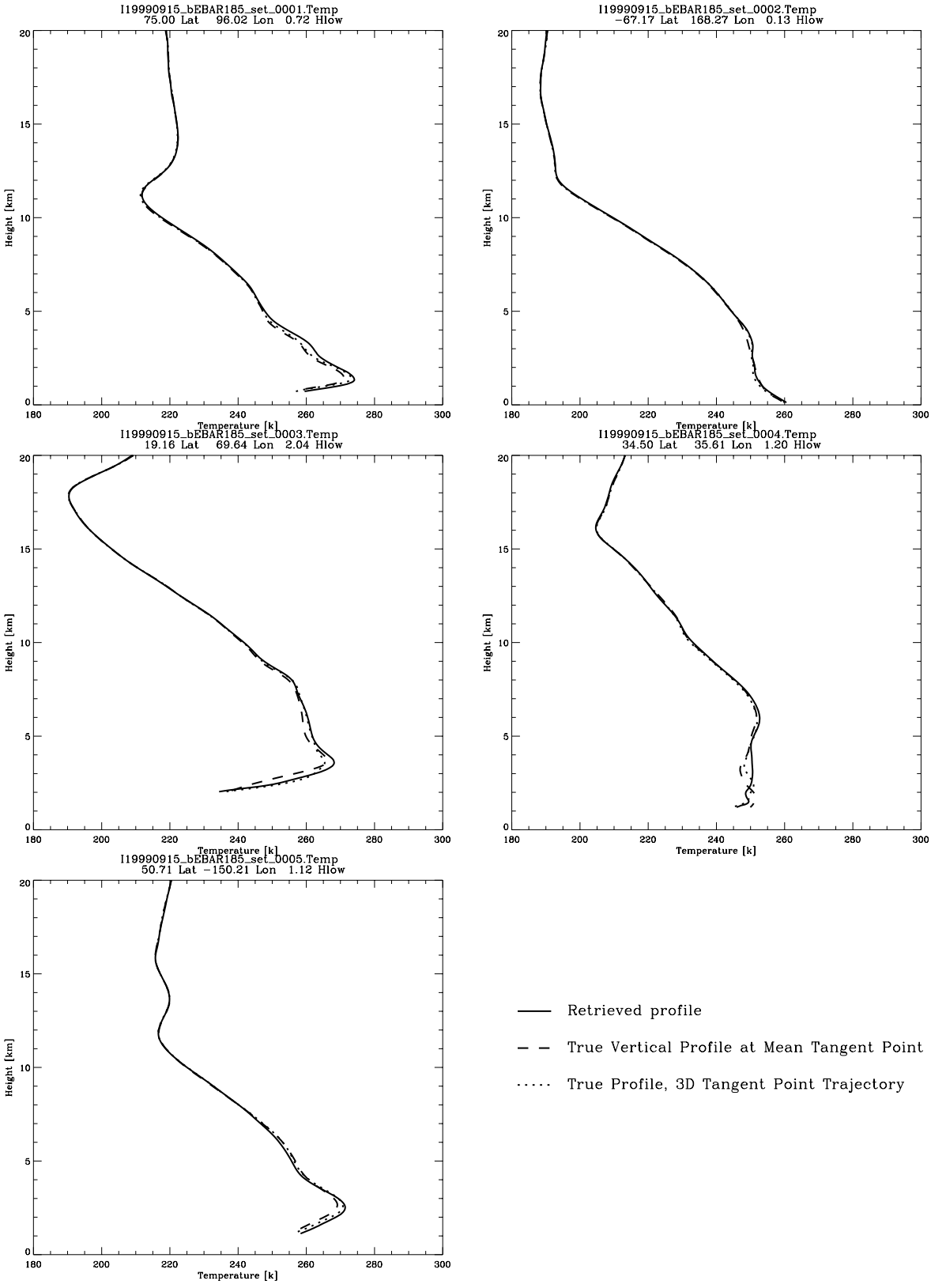

Rising Events, Az = 0 to +10 deg

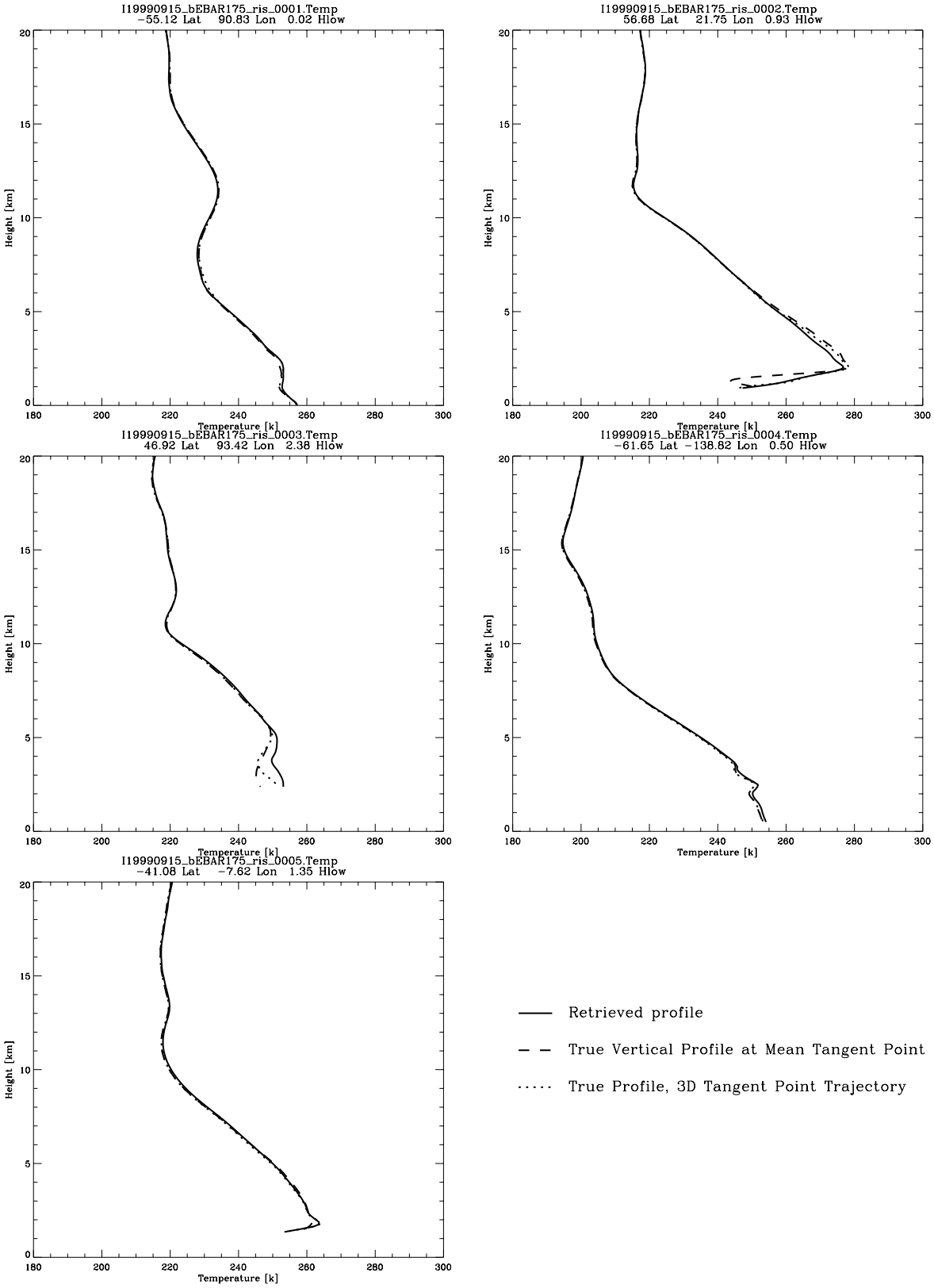

Rising Events, Az = 0 to –10 deg

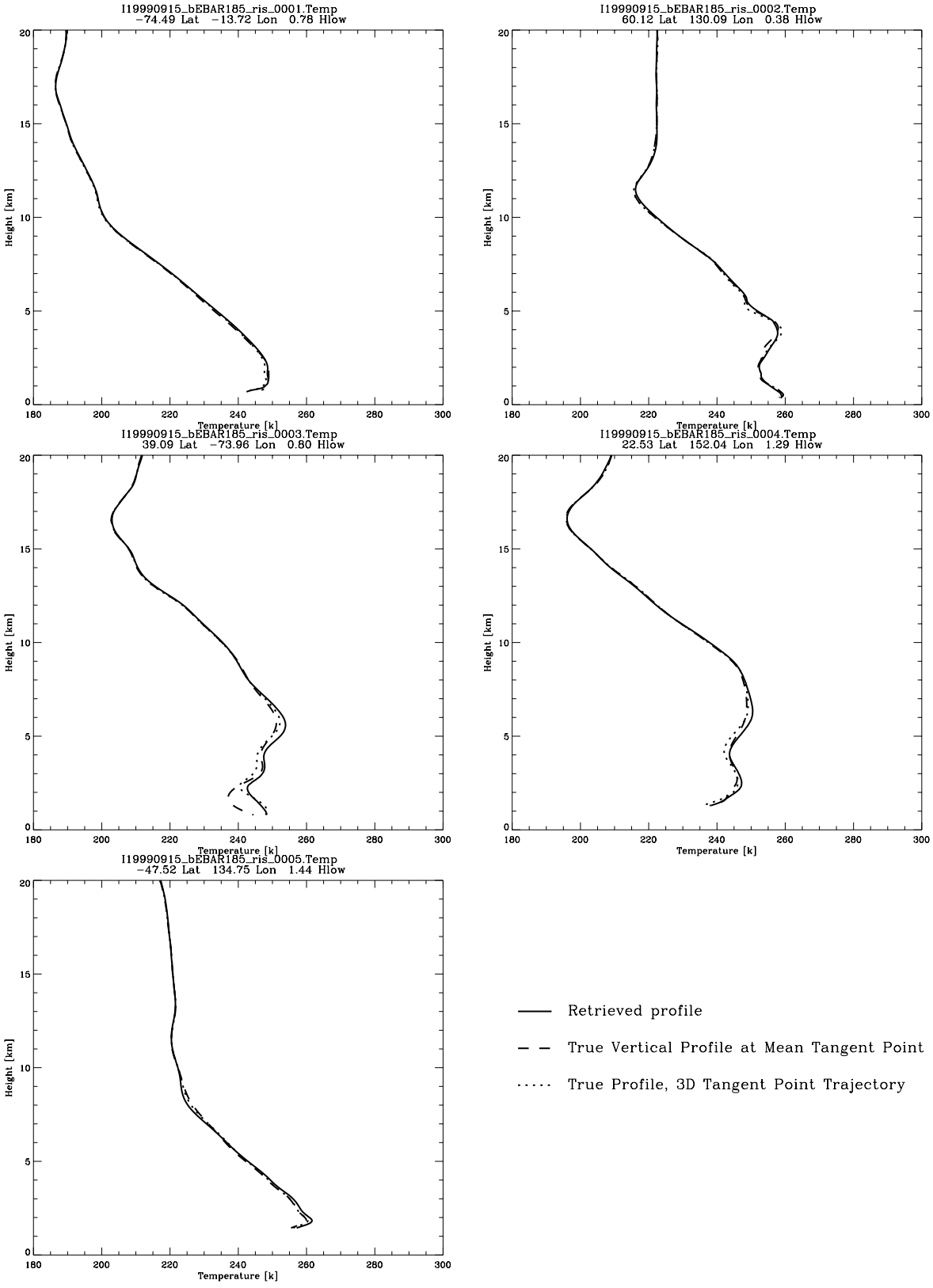

B.2. Dry Temperature Profiles, Horizontal Variability, Sector 2

Setting Events, Az = 150 – 160 deg

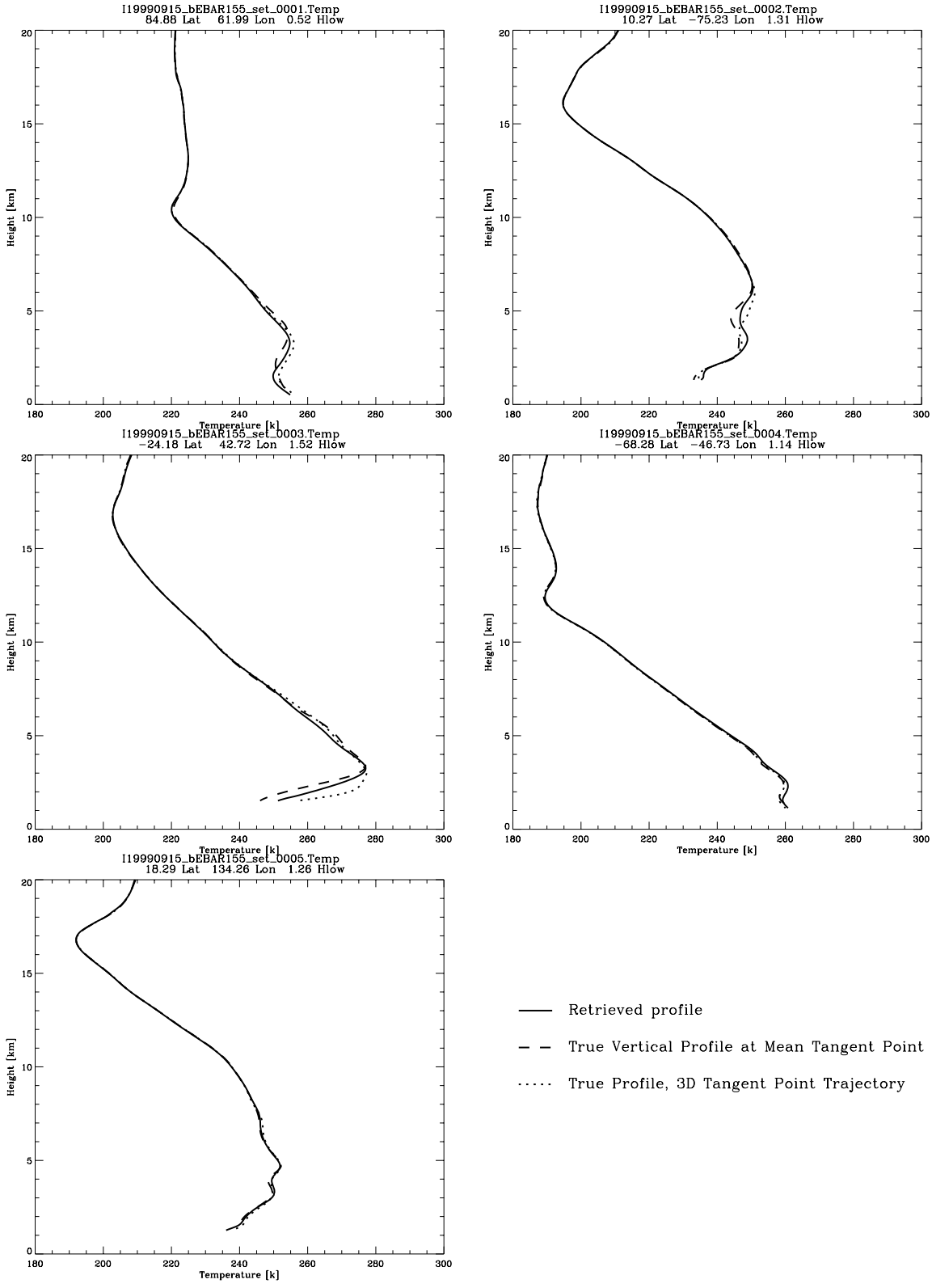

Setting Events, Az = 200 – 210 deg

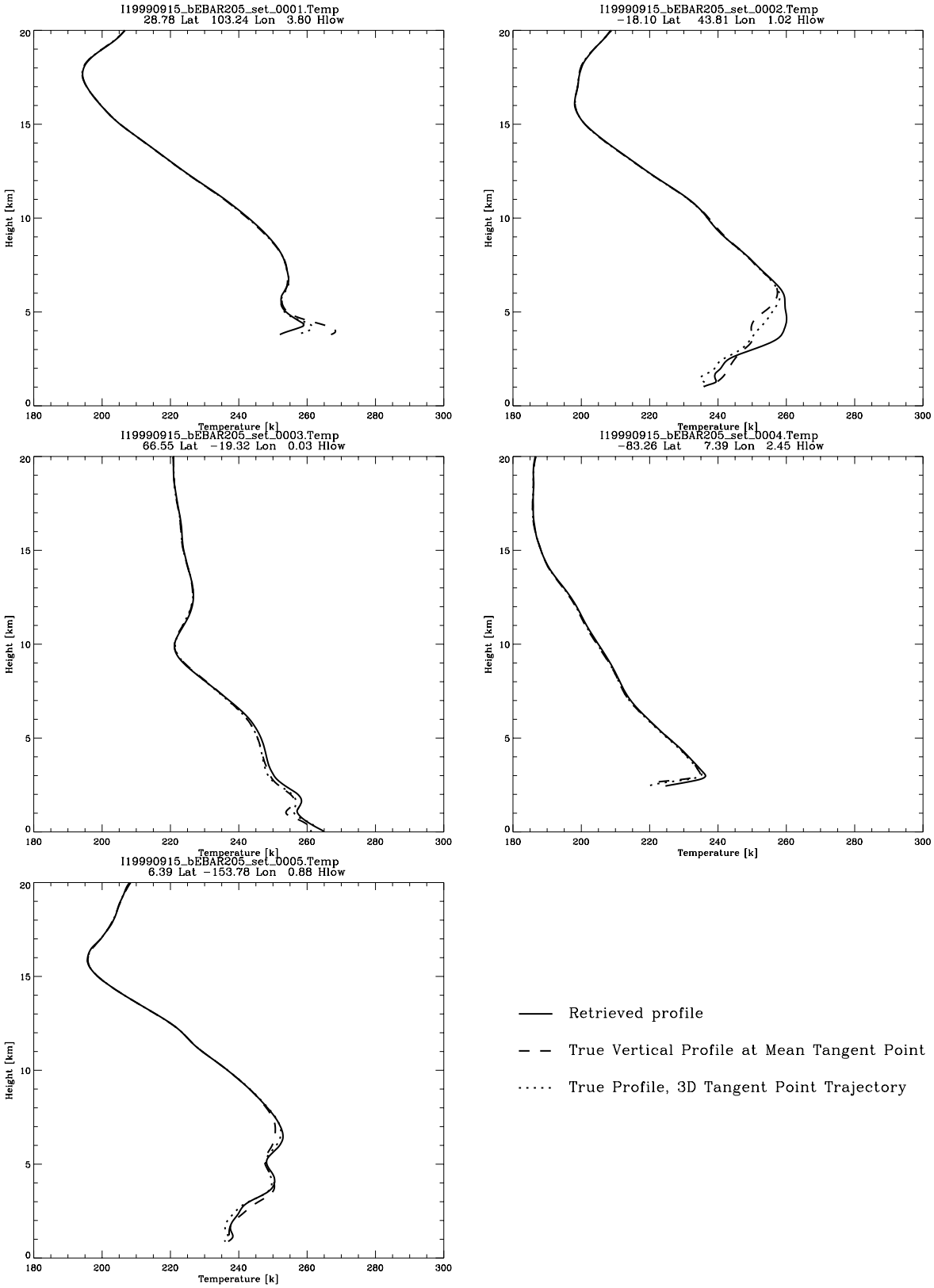

Rising Events, Az = +20 to +30 deg

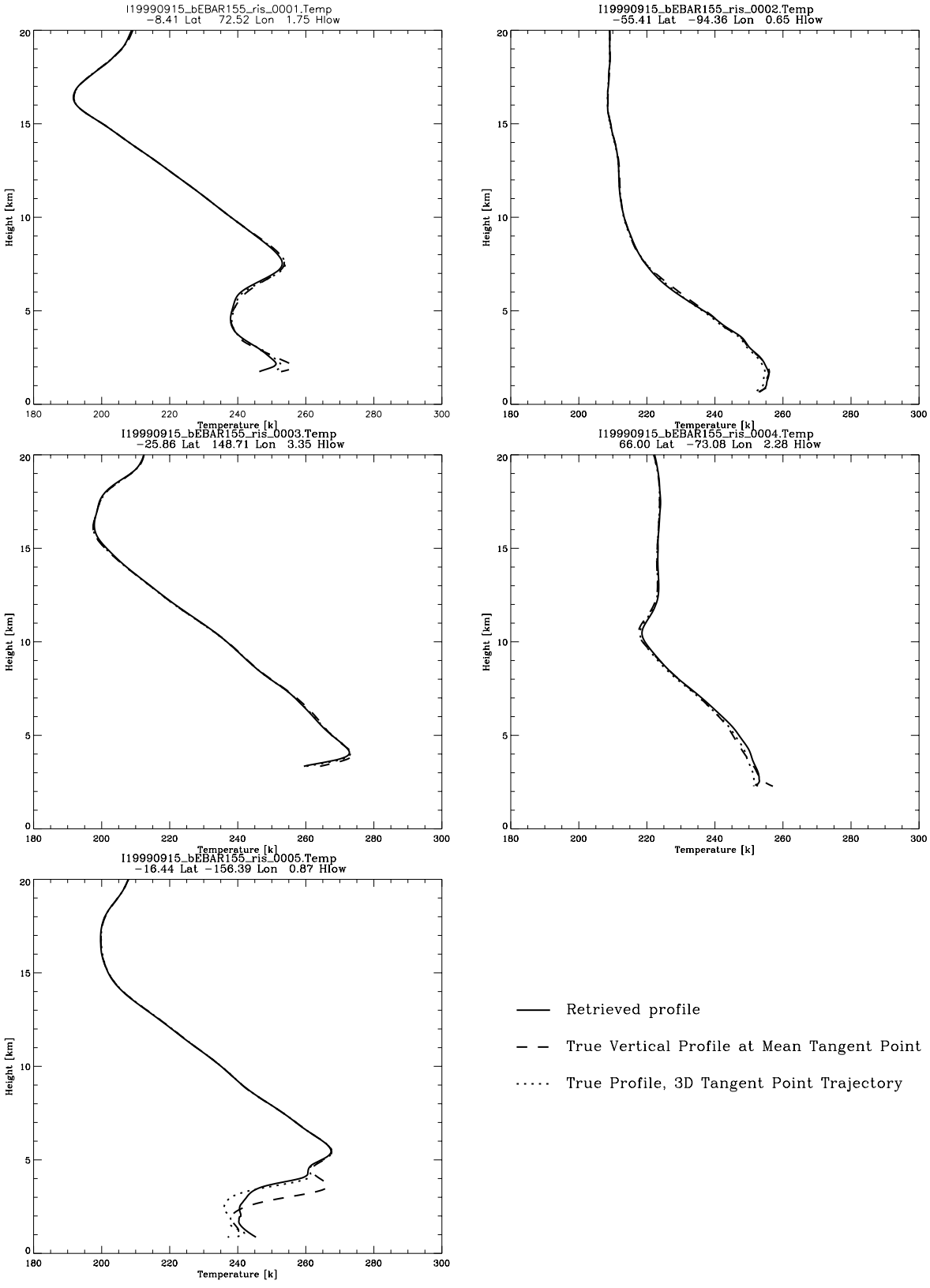

Rising Events, Az = –20 to –30 deg

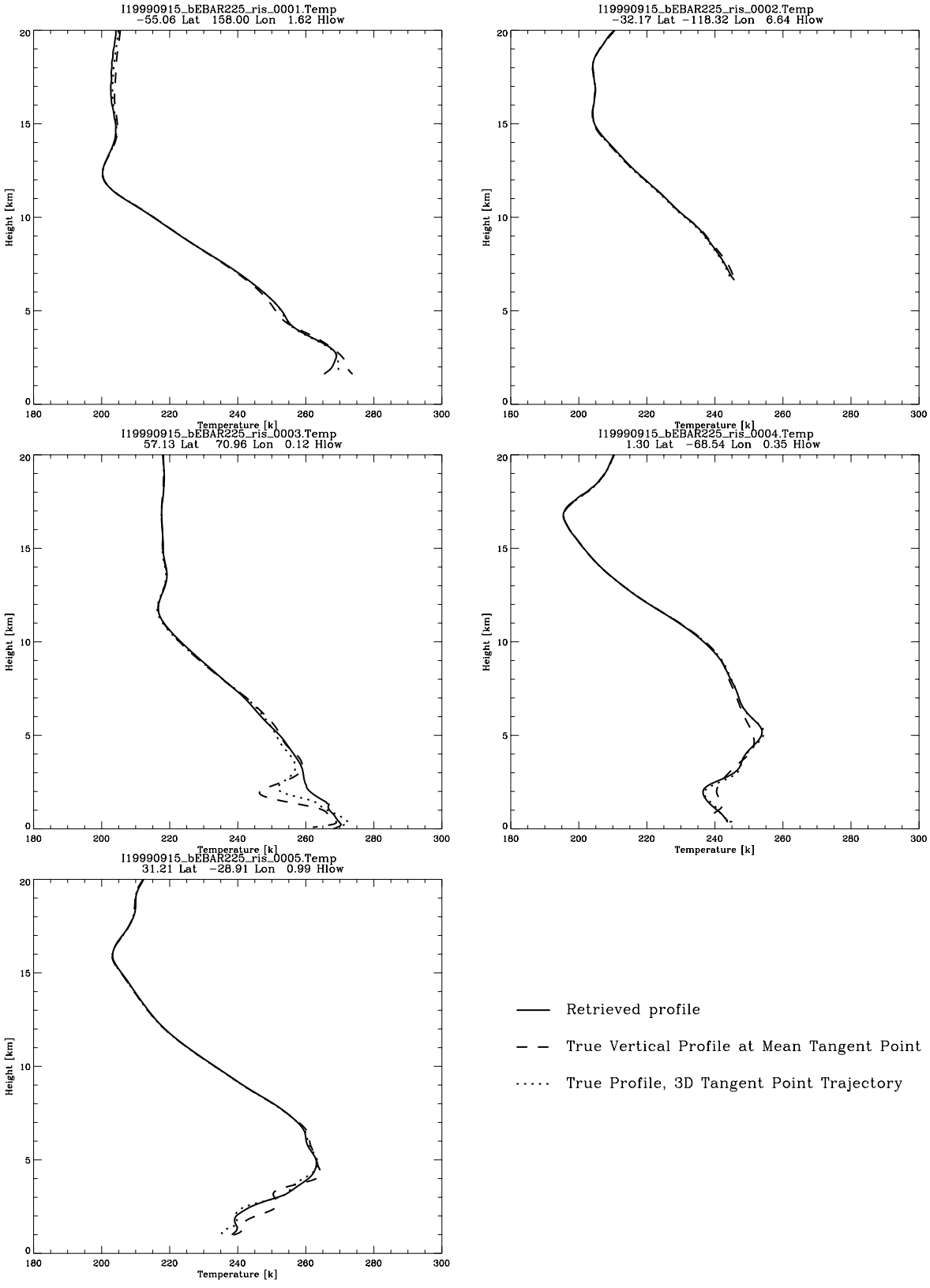

B.3. Dry Temperature Profiles, Horizontal Variability, Sector 3

Setting Events, Az = 130 – 140 deg

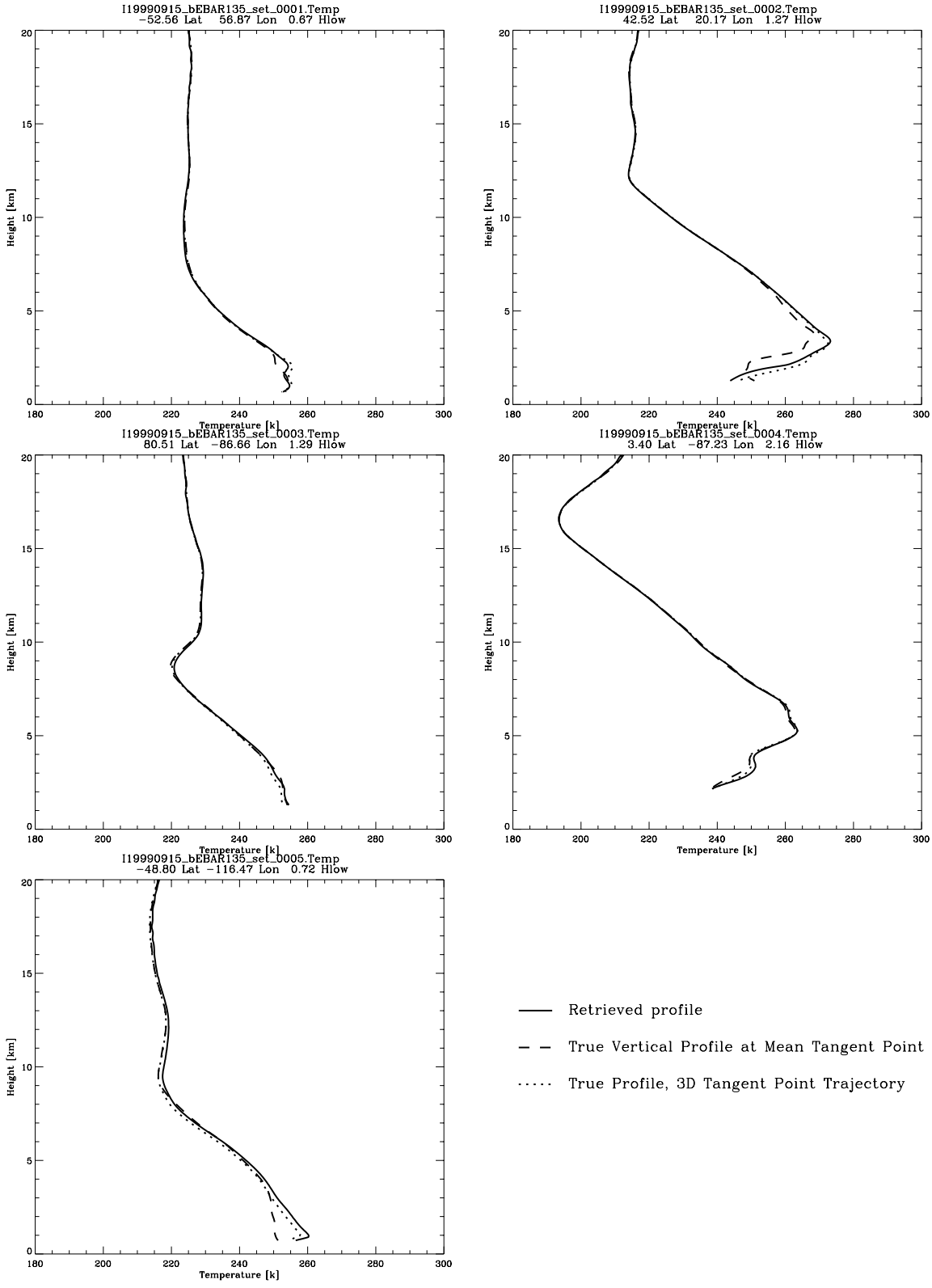

Setting Events, Az = 220 – 230 deg

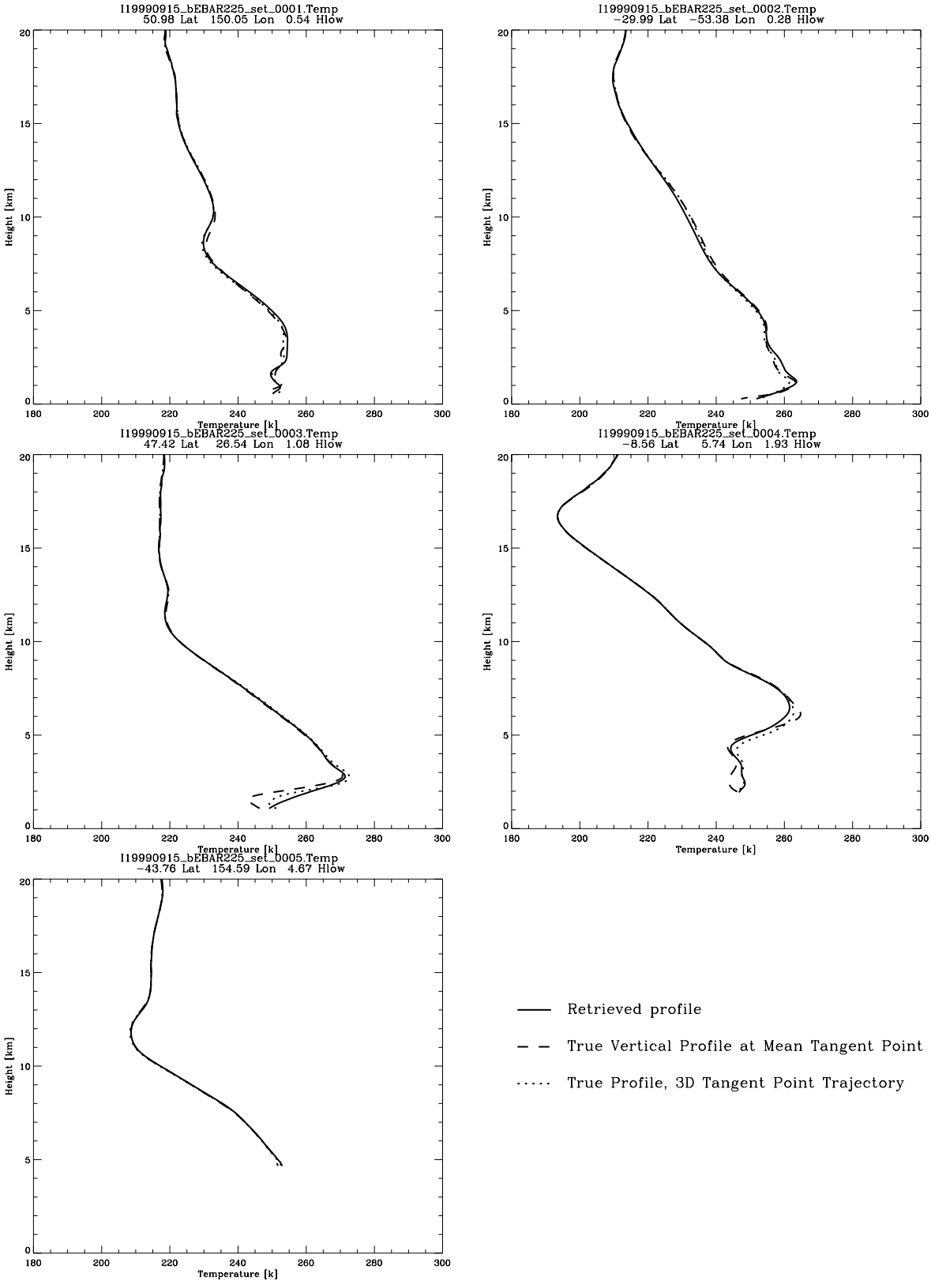

Rising Events, Az = +40 to +50 deg

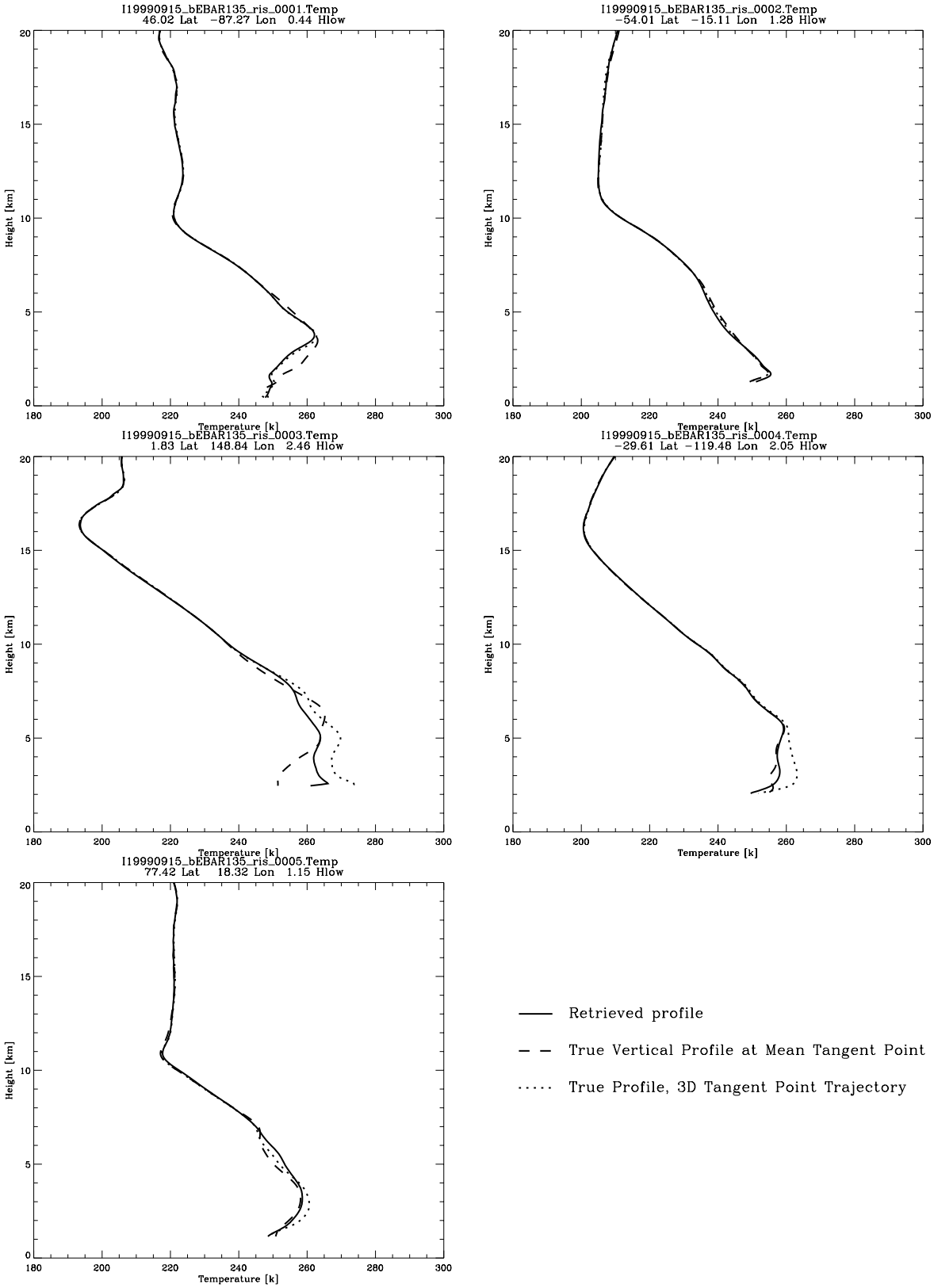

Rising Events, Az = –40 to –50 deg

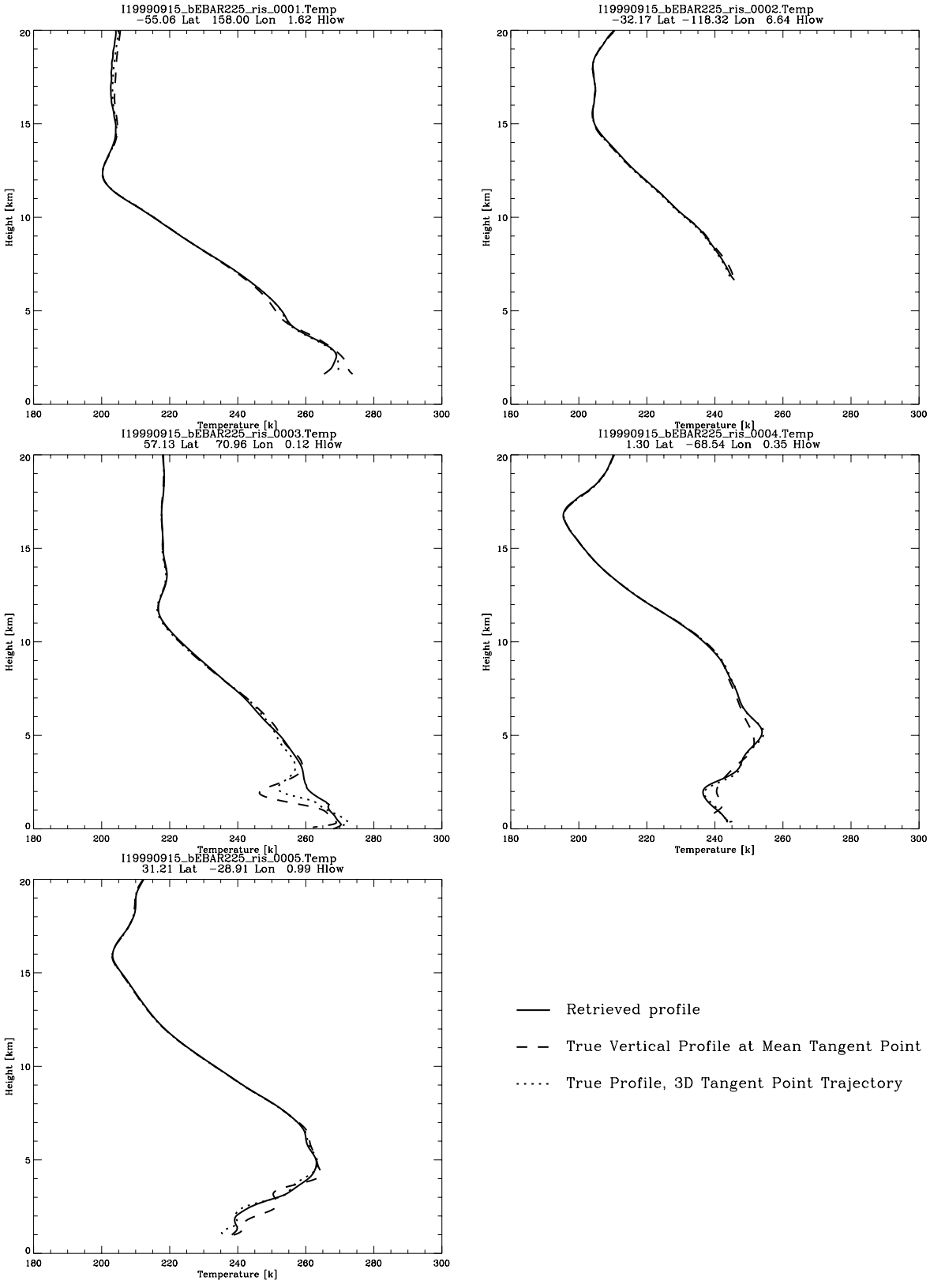

B.4. Dry Temperature Profiles, Spherical Symmetry, Sector 1

Setting Events, Az = 170 – 180 deg

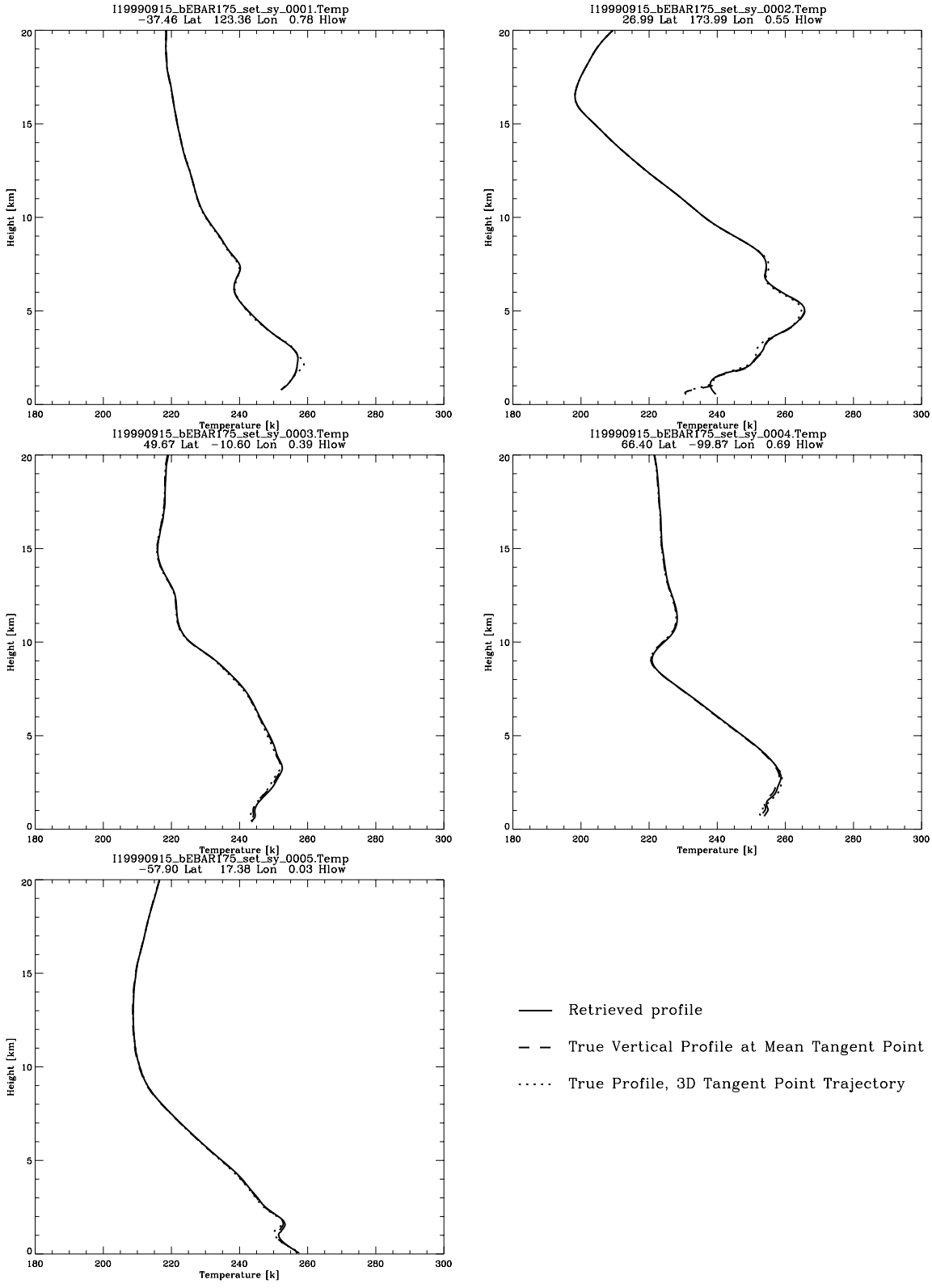

Setting Events, Az = 180 – 190 deg

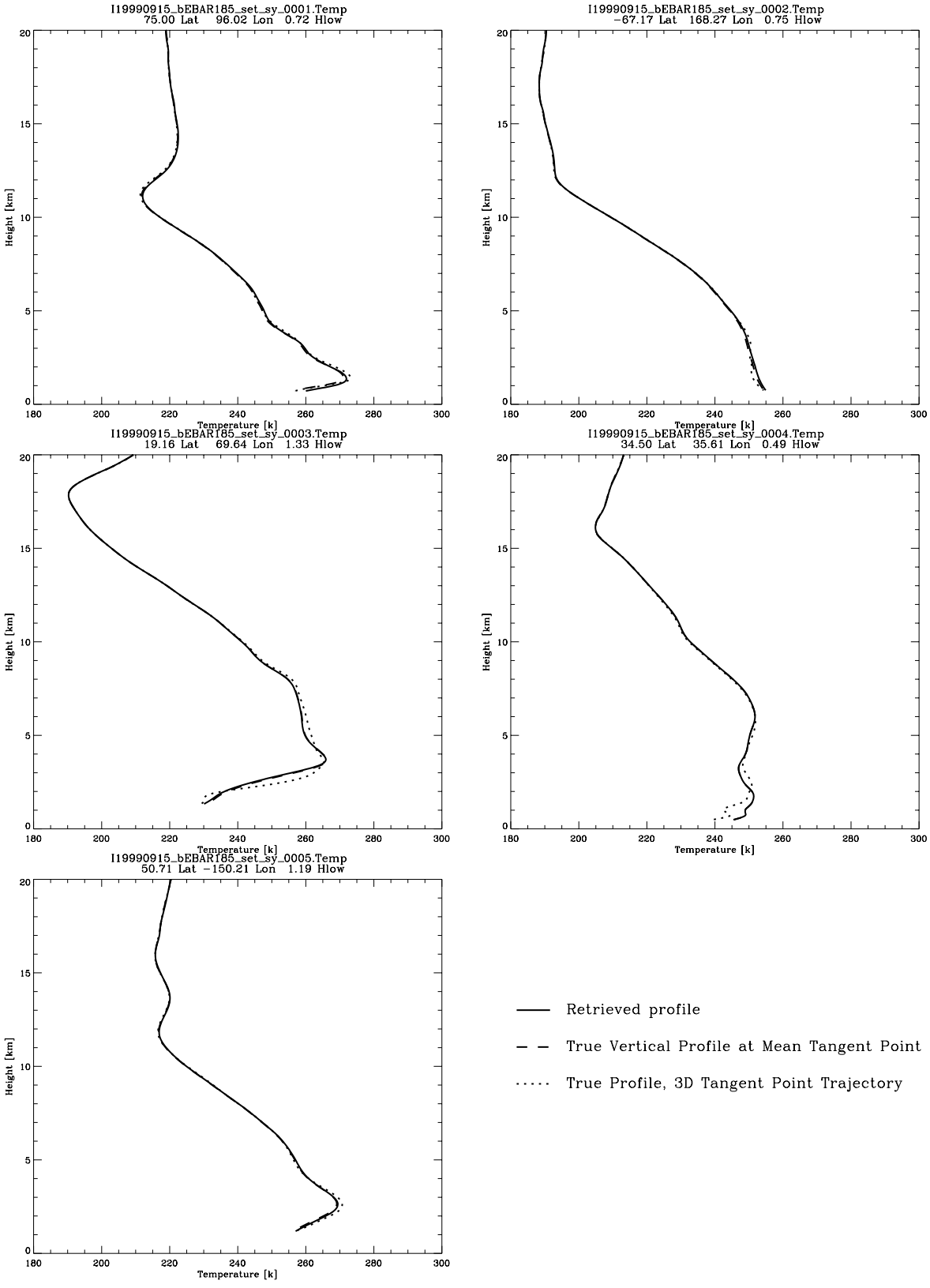

Rising Events, Az = 0 to +10 deg

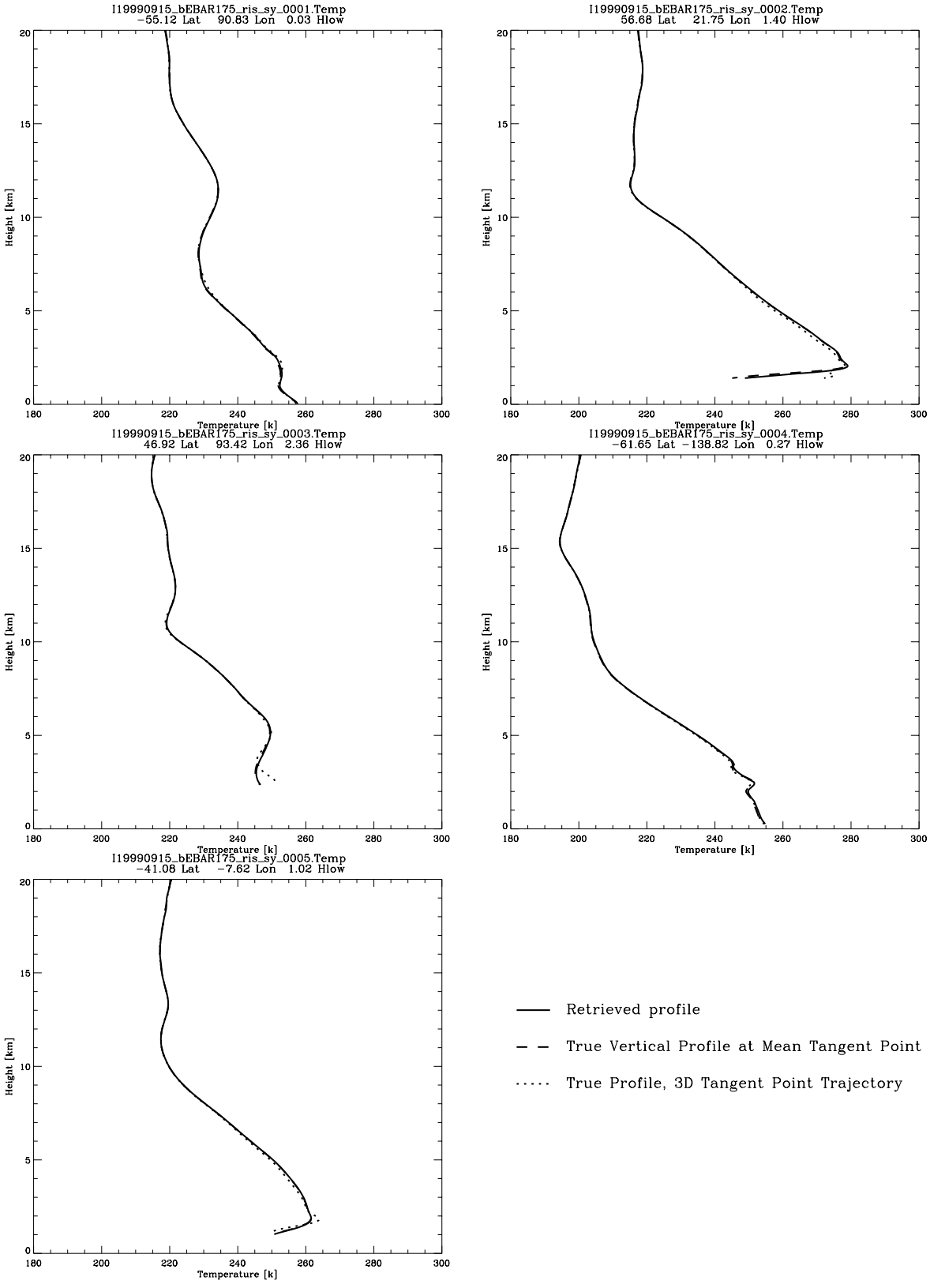

Rising Events, Az = 0 to –10 deg

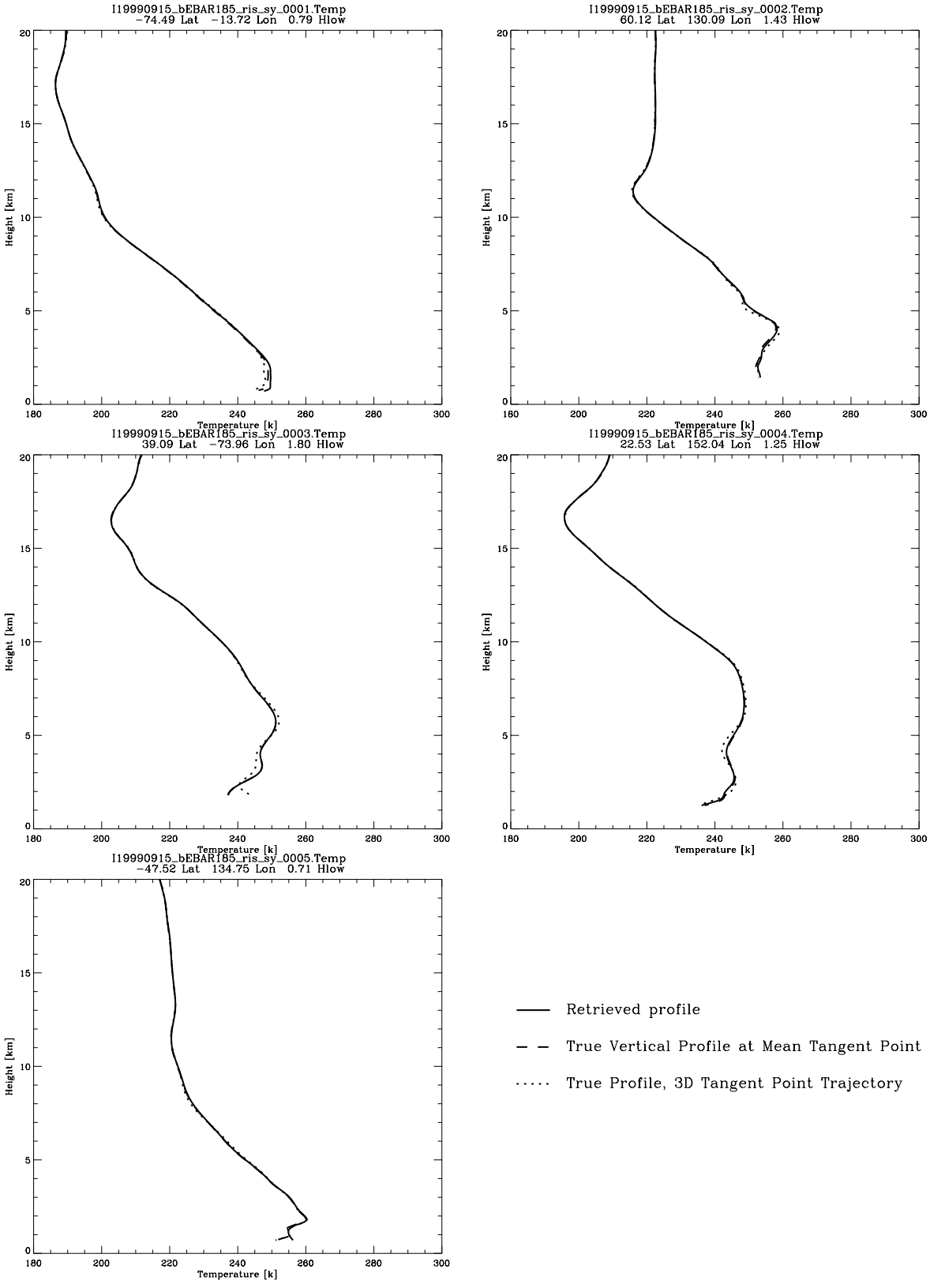

B.5. Dry Temperature Profiles, Sperical Symmetry, Sector 2

Setting Events, Az = 150 – 160 deg

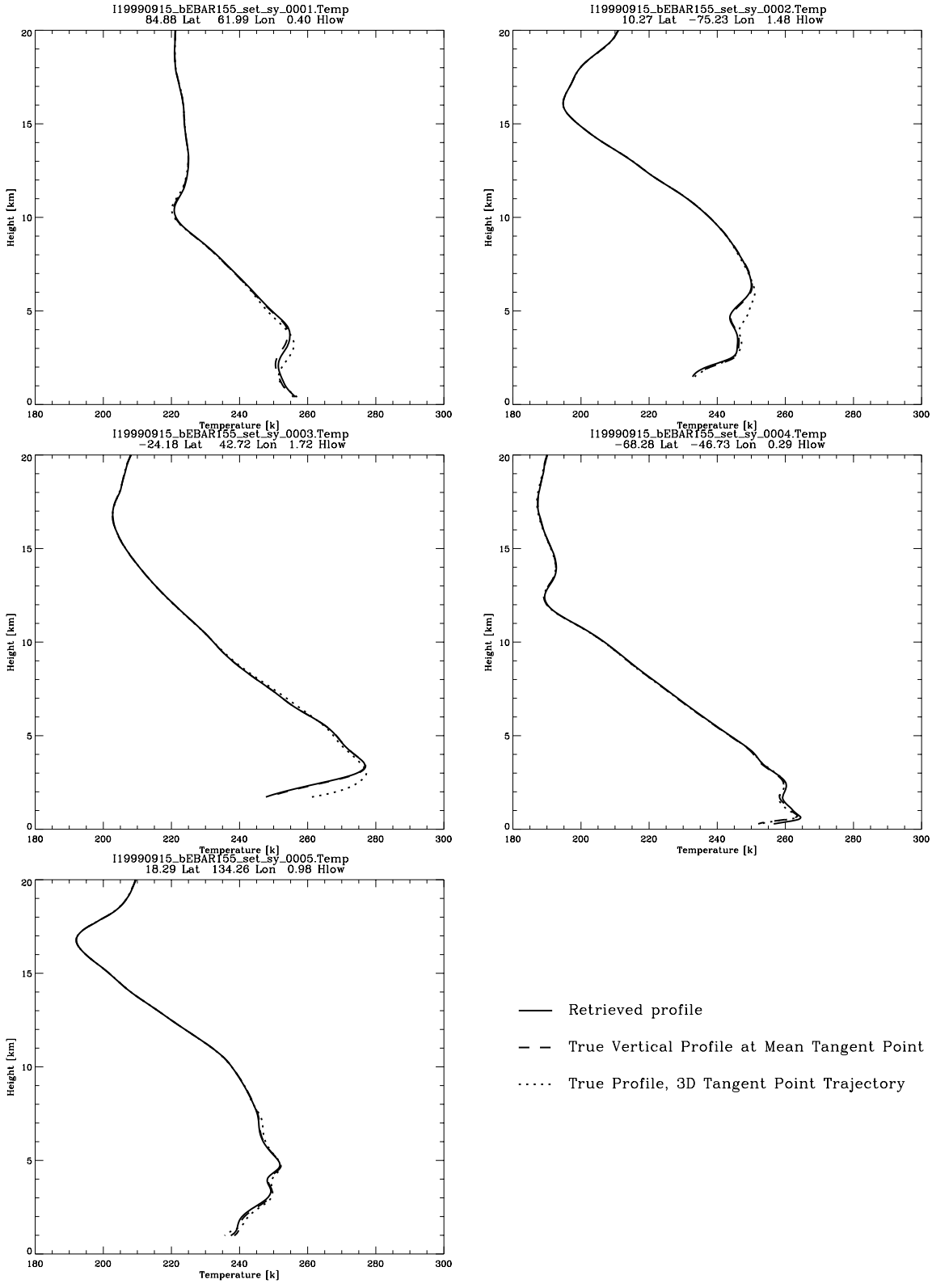

Setting Events, Az = 200 – 210 deg

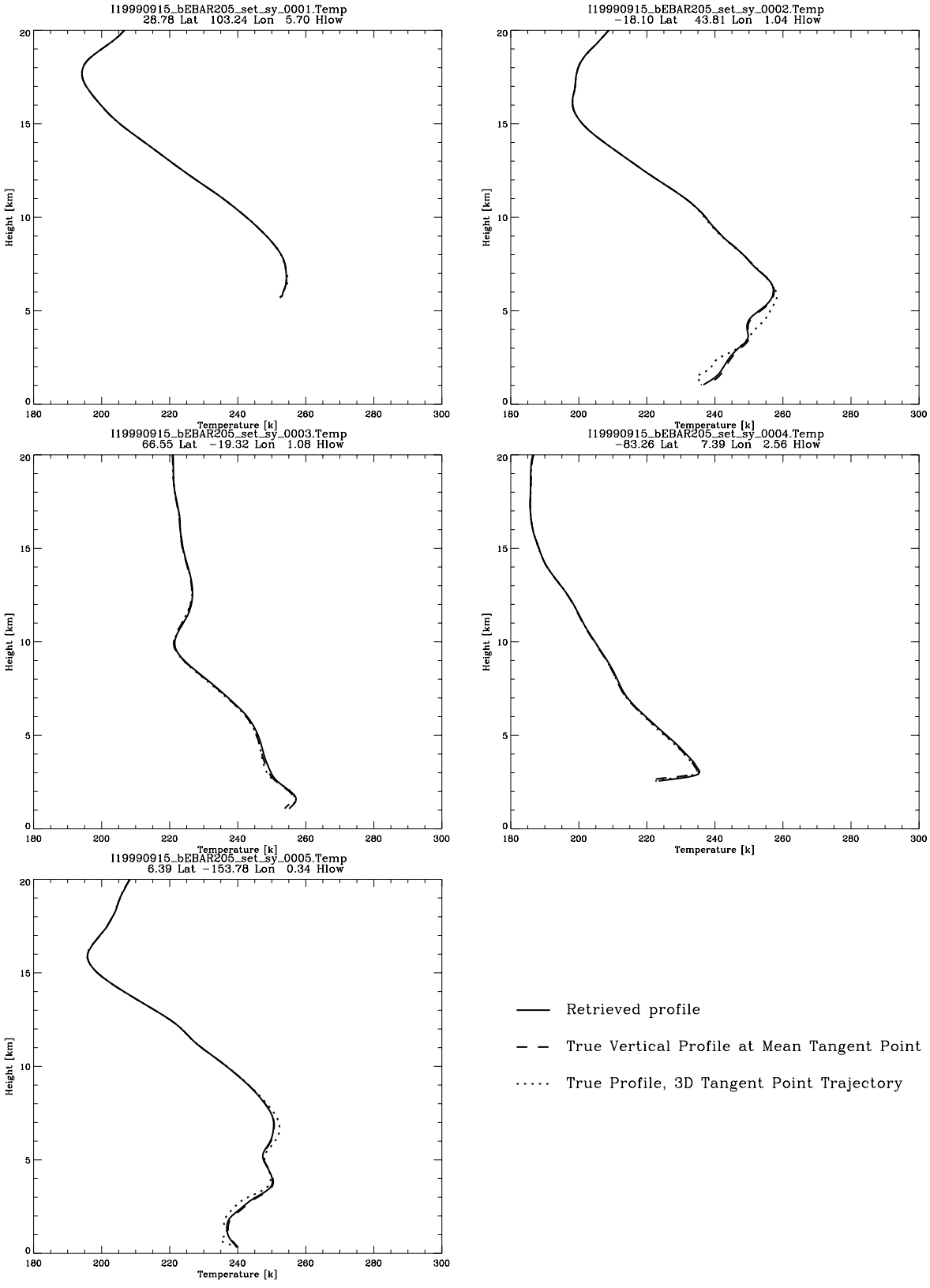

Rising Events, Az = +20 to +30 deg

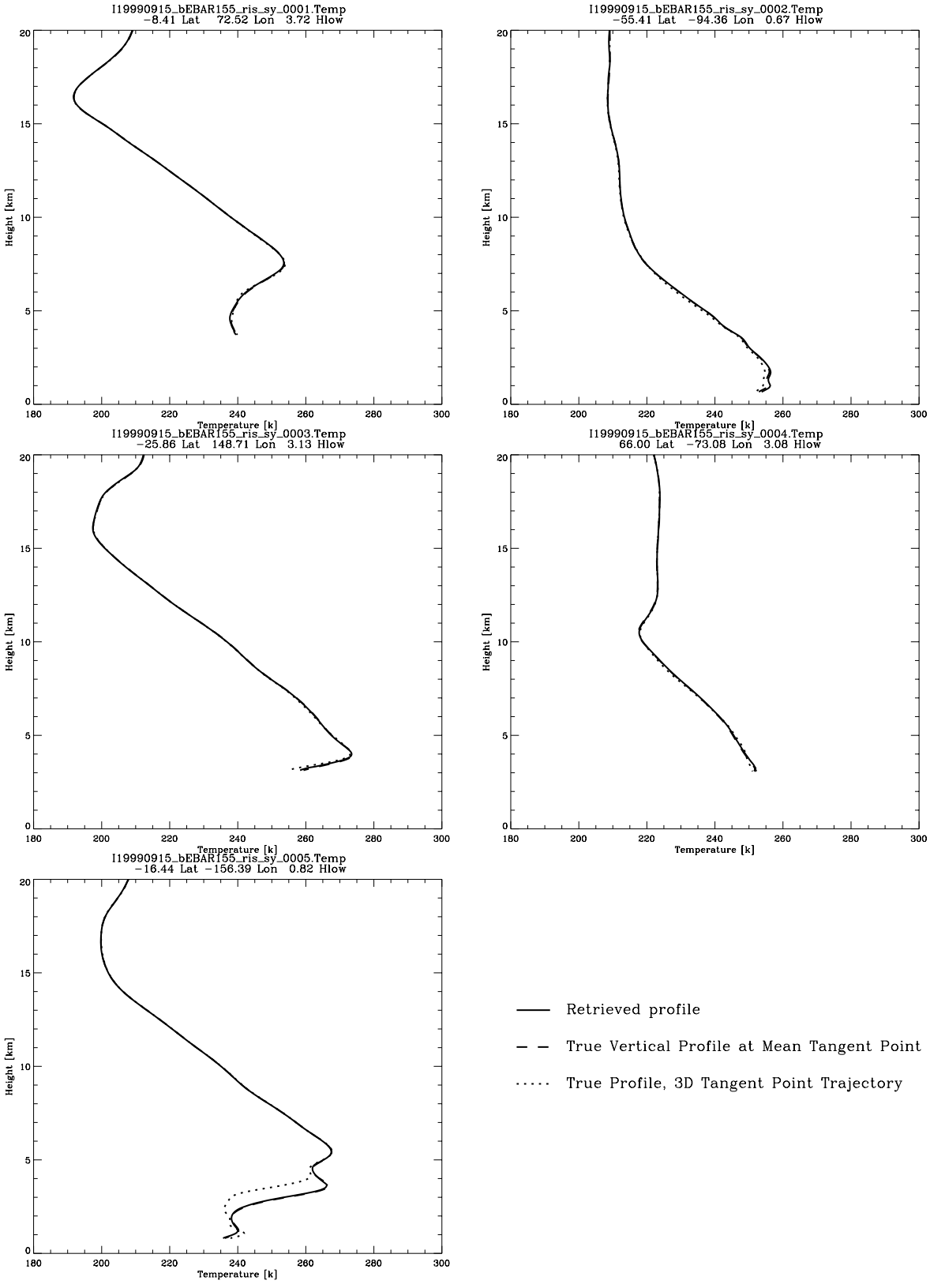

Rising Events, Az = –20 to –30 deg

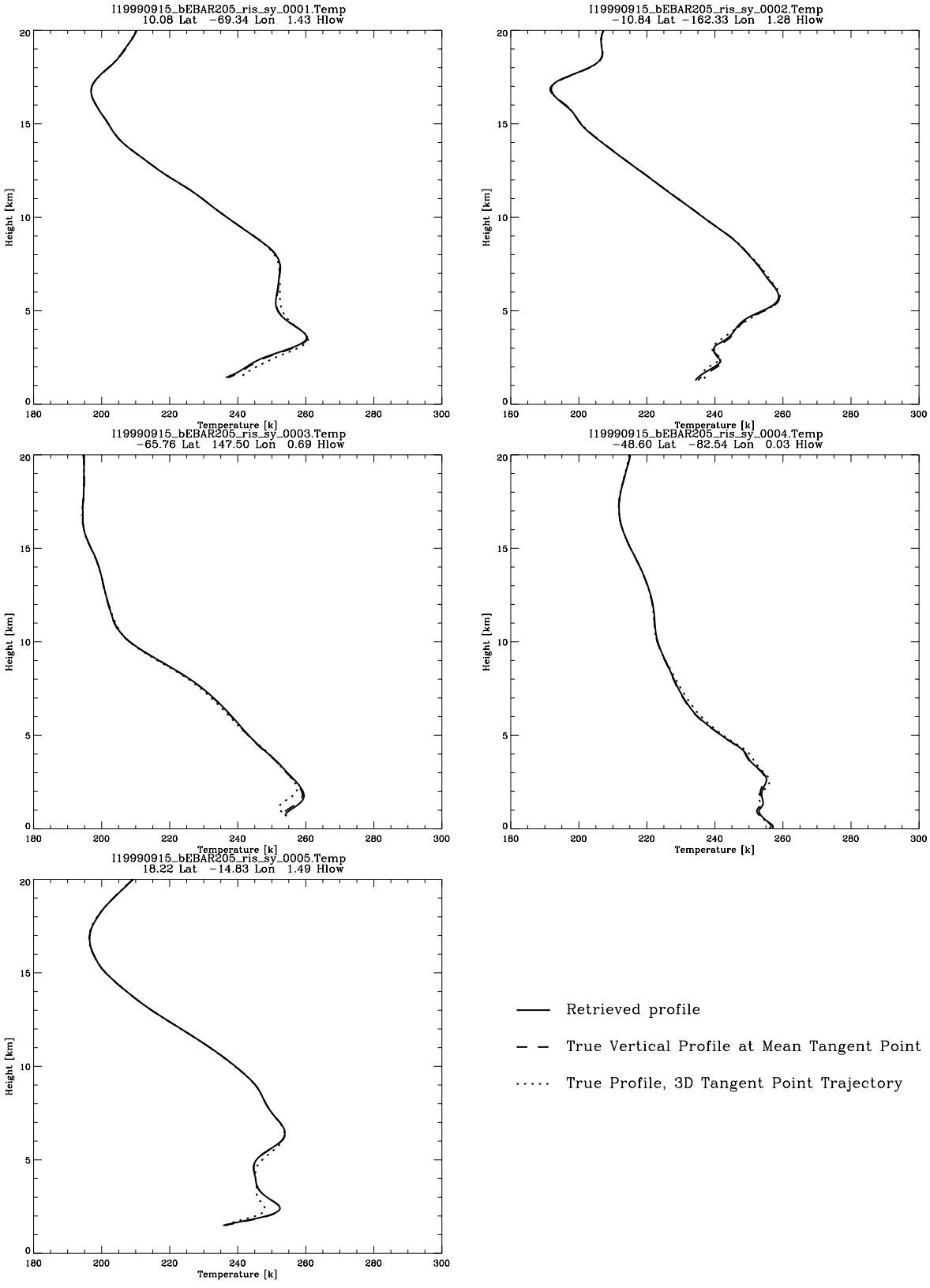

B.6. Dry Temperature Profiles, Spherical Symmetry, Sector 3

Setting Events, Az = 130 – 140 deg

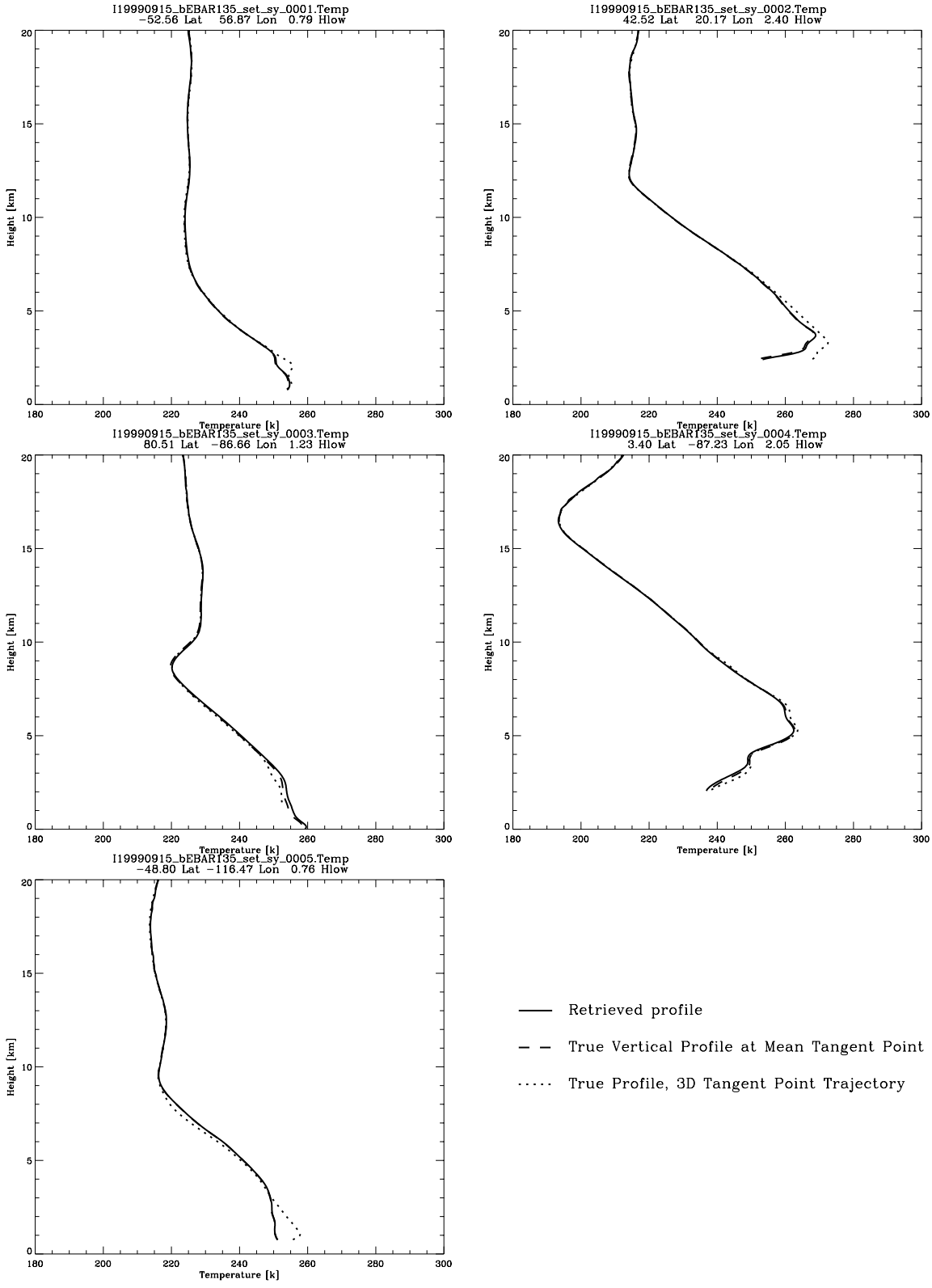

Setting Events, Az =220 – 230 deg

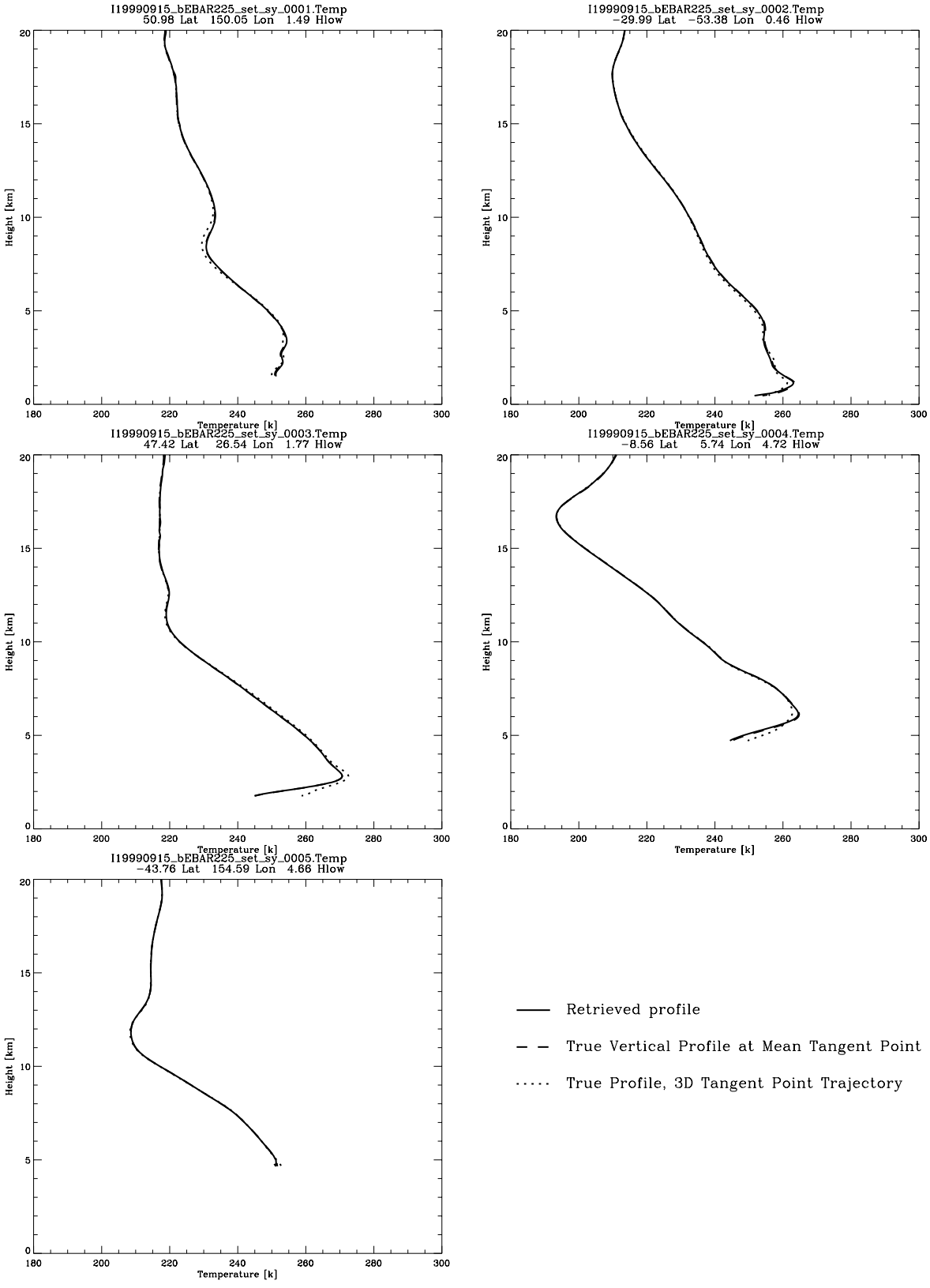

Rising Events, Az = +40 to +50 deg

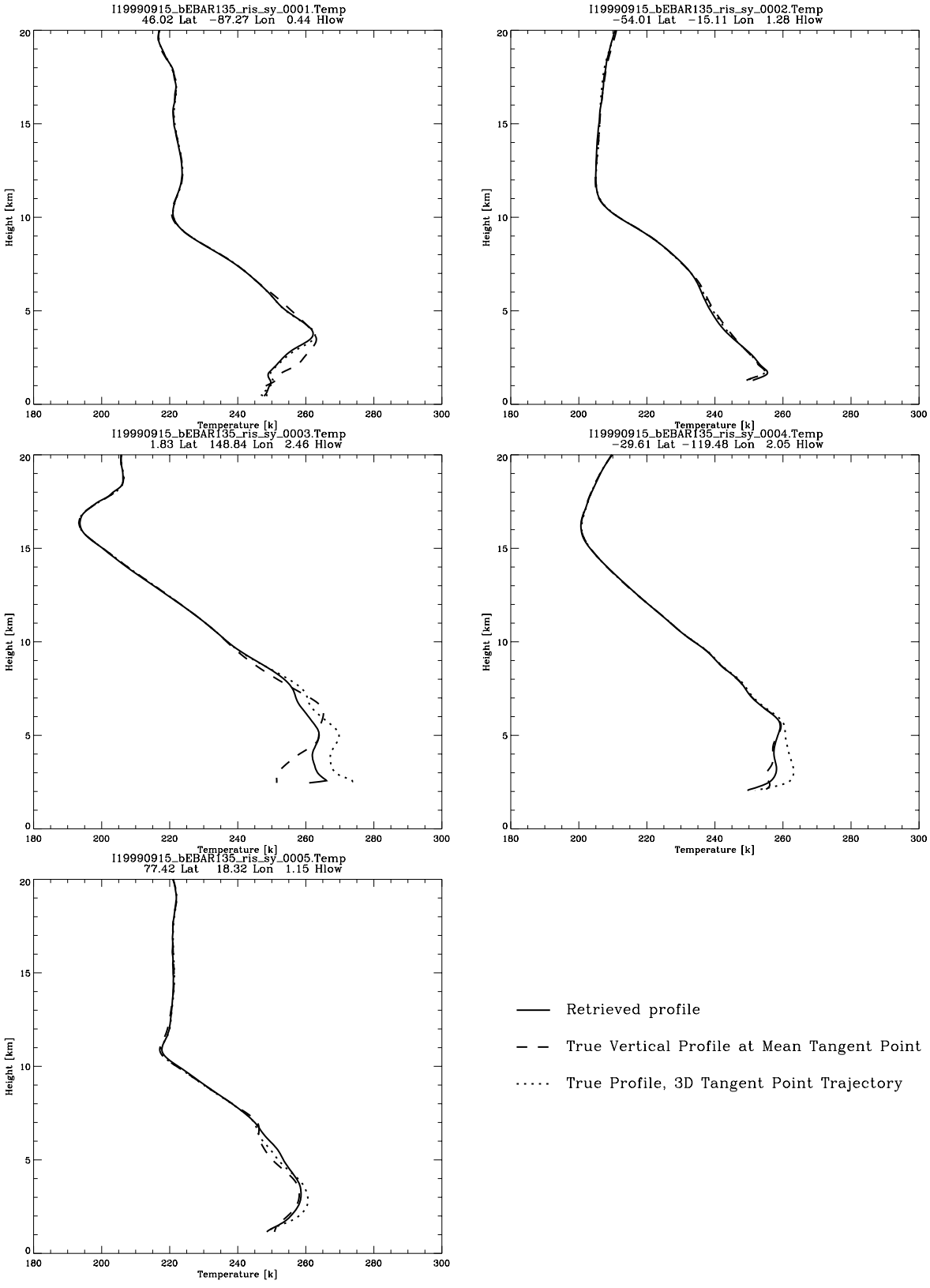

Rising Events, Az = –40 to –50 deg

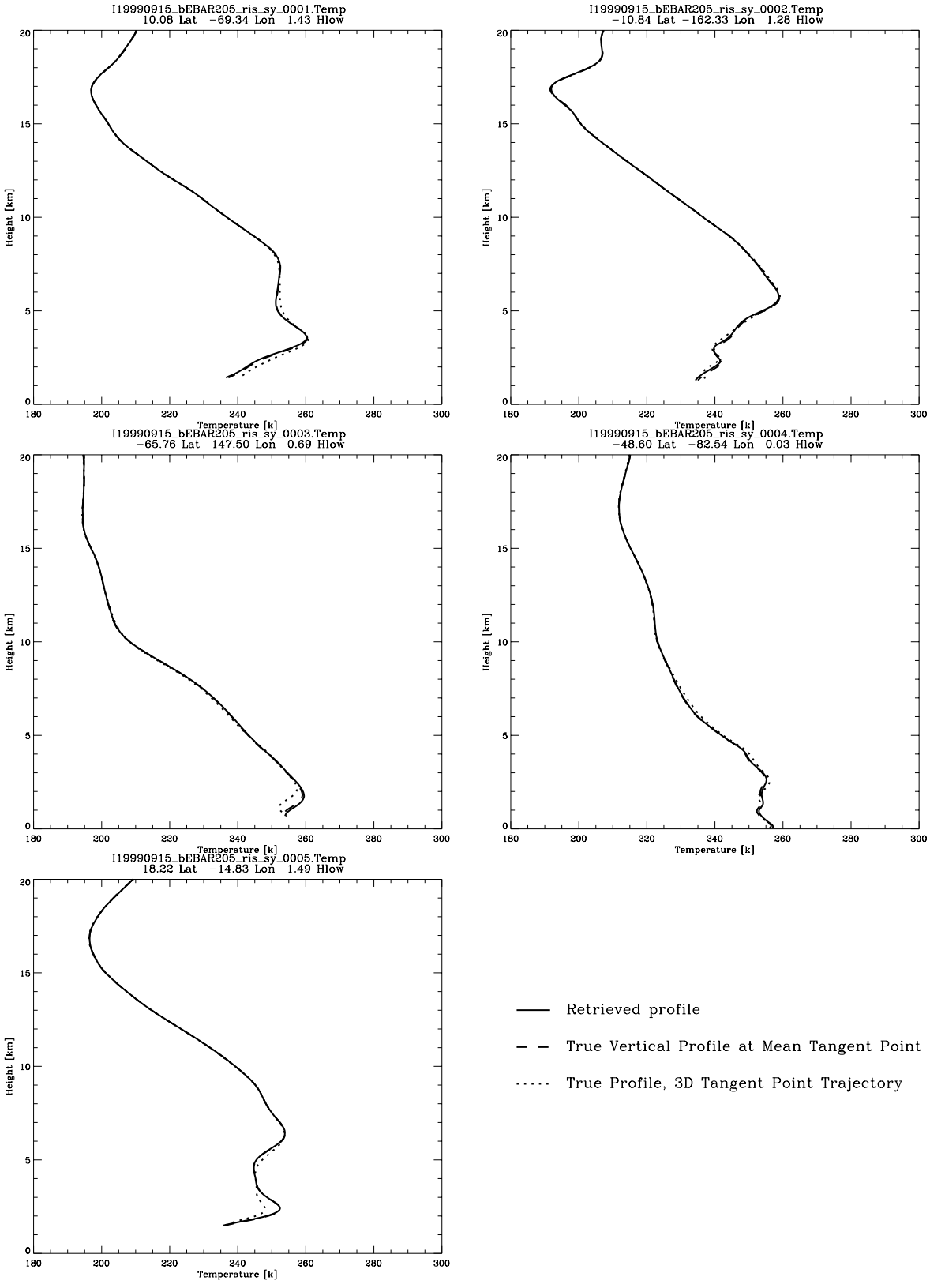

Ω end of document Ω